

MAGNETIC WREATHES IN RAPIDLY ROTATING SUNS

BENJAMIN P. BROWN

JILA and Dept. Astrophysical & Planetary Sciences, University of Colorado, Boulder, CO 80309-0440

MATTHEW K. BROWNING

Canadian Institute for Theoretical Astrophysics, University of Toronto, Toronto, ON M5S3H8 Canada

ALLAN SACHA BRUN

DSM/IRFU/SAp, CEA-Saclay and UMR AIM, CEA-CNRS-Université Paris 7, 91191 Gif-sur-Yvette, France

MARK S. MIESCH

High Altitude Observatory, NCAR, Boulder, CO 80307-3000

AND

JURI TOOMRE

JILA and Dept. Astrophysical & Planetary Sciences, University of Colorado, Boulder, CO 80309-0440

Submitted to ApJ

ABSTRACT

When our Sun was young it rotated much more rapidly than now. Observations of young, rapidly rotating stars indicate that many possess substantial magnetic activity and strong axisymmetric magnetic fields. We conduct simulations of dynamo action in rapidly rotating suns with the 3-D MHD anelastic spherical harmonic (ASH) code to explore the complex coupling between rotation, convection and magnetism. Here we study dynamo action realized in the bulk of the convection zone for two systems, one rotating at three times the current solar rotation rate and another at five times the solar rate. We find that substantial organized global-scale magnetic fields are achieved by dynamo action in these systems. Striking wreathes of magnetism are built in the midst of the convection zone, coexisting with the turbulent convection. This is a great surprise, for many solar dynamo theories have suggested that a tachocline of penetration and shear at the base of the convection zone is a crucial ingredient for organized dynamo action, whereas these simulations do not include such tachoclines. Some dynamos achieved in these rapidly rotating states build persistent global-scale fields which maintain amplitude and polarity for thousands of days. In the case at five times the solar rate, the dynamo can undergo cycles of activity, with fields varying in strength and even changing polarity. As the magnetic fields wax and wane in strength, the primary response in the convective flows involves the axisymmetric differential rotation, which begins to vary on similar time scales. Bands of relatively fast and slow fluid propagate toward the poles on time scales of roughly 500 days. In the Sun, similar patterns are observed in the poleward branch of the torsional oscillations, and these may represent a response to poleward propagating magnetic field deep below the solar surface.

Subject headings: convection – MHD – stars:interiors – stars:rotation – stars: magnetic fields – Sun:interior

1. STELLAR MAGNETISM AND ROTATION

Most stars are born rotating quite rapidly. They can arrive on the main sequence with rotational velocities as high as 200 km s^{-1} (Bouvier et al. 1997). Stars with convection zones at their surfaces, like the Sun, slowly spin down as they shed angular momentum through their magnetized stellar winds (e.g., Weber & Davis 1967; Skumanich 1972; MacGregor & Brenner 1991). The time needed for significant spindown appears to be a strong function of stellar mass (e.g., Barnes 2003; West et al. 2004): solar-mass stars slow less rapidly than somewhat less massive G and K-type stars, but still appear to lose much of their angular momentum by the time they are as old as the Sun. Present day observations of the solar wind likewise indicate that the current angular momentum flux from the Sun is a few times 10^{30} dyn cm (e.g., Pizzo et al. 1983), suggesting a time scale for substantial angular momentum loss of a few billion years. Thus the Sun likely rotated significantly more rapidly in its youth than it

does today.

1.1. Rotation-Activity Relations

Rotation appears to be inextricably linked to stellar magnetic activity. Observations indicate that in stars with extensive convective envelopes, chromospheric and coronal activity – which partly trace magnetic heating of stellar atmospheres – first rise with increasing rotation rate, then eventually level off at a constant value for rotation rates above a mass-dependent threshold velocity (e.g., Noyes et al. 1984; Delfosse et al. 1998; Pizzolato et al. 2003). Activity may even decline somewhat in the most rapid rotators (e.g., James et al. 2000). Similar correspondence is observed between rotation rate and estimates of the unsigned surface magnetic flux (Saar 1996, 2001; Reiners et al. 2009). This “rotation-activity” relationship is tightened when stellar rotation is given in terms of the Rossby number $Ro \sim P/\tau_c$, with P the rotation period and τ_c an estimate of the convective overturning time (e.g., Noyes et al. 1984). Expressed in this fashion, a common rotation-activity correlation appears to span spectral types

ranging from late F to late M (e.g., Mohanty & Basri 2003; Pizzolato et al. 2003; Reiners & Basri 2007). Magnetic fields can likewise feed back upon stellar rotation by modifying the rate at which angular momentum is lost through a stellar wind (e.g., Weber & Davis 1967; Matt & Pudritz 2008). Analyses of stellar spindown as a function of age and mass have thus provided further constraints on stellar magnetism and its connections to rotation. In addition, recent observations of solar-type stars may indicate that topology of the global-scale fields changes with rotation rate, with the rapid rotators having substantial global-scale toroidal magnetic fields at their surfaces (Petit et al. 2008). The overall picture that emerges from these observations is that rapid rotation, as realized in the younger Sun and in a host of other stars, can aid in the generation of strong magnetic fields and that young stars tend to be rapidly rotating and magnetically active, whereas older ones are slower and less active (e.g., Barnes 2003; West et al. 2004, 2008).

A full theoretical understanding of the rotation-activity relationship, and likewise of stellar spindown, has remained elusive. Some aspects of these phenomena probably depend upon the details of magnetic flux emergence, chromospheric and coronal heating, and mass loss mechanisms – but the basic *existence* of a rotation-activity relationship is widely thought to reflect some underlying rotational dependence of the dynamo process itself (e.g., Knobloch et al. 1981; Noyes et al. 1984; Baliunas et al. 1996).

1.2. Elements of Global Dynamo Action

In stars like the Sun, the global-scale dynamo is generally thought to be located in the tachocline, an interface of shear between the differentially rotating convection zone and the radiative interior which is in solid body rotation (e.g., Parker 1993; Charbonneau & MacGregor 1997; Ossendrijver 2003). Helioseismology revealed the internal rotation profile of the Sun and the presence of this important shear layer (e.g., Thompson et al. 2003). The stably stratified tachocline may also provide a region for storing and amplifying coherent tubes of magnetic field which may eventually rise to the surface of the Sun as sunspots. It has generally been believed that magnetic buoyancy instabilities may prevent fields from being strongly amplified within the bulk of the convection zone itself (Parker 1975). In the now prevalent “interface dynamo” model, solar magnetic fields are partly generated in the convection zone by helical convection, then transported downward into the tachocline where they are organized and amplified by the shear. Ultimately the fields may become unstable and rise to the surface.

Although the rotational dependence of this process is not well understood, some guidance may come from mean-field dynamo theory. In such theories, the solar dynamo is referred to as an “ α - Ω ” dynamo, with the α -effect characterizing the twisting of fields by helical convection (e.g., Moffatt 1978; Steenbeck et al. 1966), and the Ω -effect representing the shearing of poloidal fields by differential rotation to form toroidal fields. Both of these effects are, in mean-field theory, sensitive to rotation – the α -effect because it is proportional to the kinetic helicity of the convective flows, which sense the overall rotation rate, and the Ω -effect because more rapidly rotating stars are generally expected to have stronger differential rotation. But the detailed nature of these effects in the solar dynamo and the appropriate scaling with rotation has been very difficult to elucidate.

Simulations of the global-scale solar dynamo have gener-

ally affirmed the view that the tachocline may play a central role in building the globally-ordered magnetism in the Sun. Early three-dimensional (3D) simulations of solar convection without a tachocline at the base of the convection zone achieved dynamo action and produced magnetic fields which were strongly dominated by fluctuating components with little global-scale order (Brun et al. 2004). When a tachocline of penetration and shear was included, remarkable global-scale structures were realized in the tachocline region, while the convection zone remained dominated by fluctuating fields (Browning et al. 2006). These simulations are making good progress toward clarifying the elements at work in the operation of the solar global-scale dynamo, but for other stars many questions remain. In particular, observations of large-scale magnetism in fully convective M-stars (Donati et al. 2006), along with the persistence of a rotation-activity correlation in such low-mass stars, hint that perhaps tachoclines may not be essential for the generation of global-scale magnetic fields. This view is partly borne out by simulations of M-dwarfs under strong rotational constraints (Browning 2008), where strong longitudinal mean fields were realized despite the lack of either substantial differential rotation or a stable interior and thus no classical tachocline. Major puzzles remain in the quest to understand stellar magnetism and its scaling with stellar rotation.

1.3. Convection and Dynamos in Rapidly Rotating Systems

We began our study of rapidly rotating suns by carrying out a suite of 3D hydrodynamic simulations in full spherical shells that explored the coupling of rotation and convection in these younger solar-type stars (Brown et al. 2008). Those simulations studied the influence of rotation on the patterns of convection and the nature of global-scale flows in such stars. The shearing flows of differential rotation generally grow in amplitude with more rapid rotation, possessing rapid equators and slower poles, while the meridional circulations weaken and break up into multiple cells in radius and latitude. More rapid rotation can also substantially modify the patterns of convection in a surprising fashion. With more rapid rotation, localized states begin to appear in which the convection at low latitudes is modulated in its strength with longitude. At the highest rotation rates, the convection can become confined to active nests which propagate at distinct rates and persist for long epochs.

Motivated by these discoveries, we turn here to explorations of the possible dynamo action achieved in solar-type stars rotating at three and five times the current solar rate. These 3D magnetohydrodynamic (MHD) simulations span the convection zone alone, as the nature of tachoclines in more rapidly rotating suns is at present unclear. We shall show that a variety of dynamos can be excited, including steady and oscillating states, and that dynamo action is substantially easier to achieve at these faster rotation rates than in the solar simulations. Magnetism leads to strong feedbacks on the flows, particularly modifying the differential rotation and its scaling with overall rotation rate Ω_0 . The magnetic fields which form in these dynamos have prominent global-scale organization within the convection zone, in contrast to previous solar dynamo simulations (Brun et al. 2004; Browning et al. 2006). Quite strikingly, we find that coherent global magnetic structures arise naturally in the midst of the turbulent convection zones. These wreath-like structures are regions of strong longitudinal field B_ϕ organized loosely into tubes, with fields wandering in and out of the surrounding convection. These

wreathes of magnetism differ substantially from the idealized flux tubes supposed in many dynamo theories, though they may be related to coherent structures achieved in local simulations of dynamo action in shear flows (Cline et al. 2003; Vasil & Brummell 2008, 2009). Here we explore the nature of magnetic wreathes realized in our global simulations, and discuss their temporal behavior.

We outline in §2 the 3D MHD anelastic spherical shell model and the parameter space explored by these simulations. We then examine in §§3 and 4 the structure of magnetic fields found in rapidly rotating dynamo at three times the solar rate, which builds remarkable global-scale ordered fields in the midst of its convection zone. In §§5-6 we explore time varying behavior and organized global-scale polarity reversals in a dynamo rotating at five times the current solar rate. In §7 we return to the three solar case and examine how such global-scale fields are created and maintained. We reflect on our findings in §8.

2. GLOBAL MODELLING APPROACH

To study the coupling between rotation, magnetism and the large-scale flows achieved in stellar convection zones, we must employ a global model which simultaneously captures the spherical shell geometry and admits the possibility of zonal jets and large eddy vortices, and of convective plumes that may span the depth of the convection zone. The solar convection zone is intensely turbulent and microscopic values of viscosity and magnetic and thermal diffusivities in the Sun are estimated to be very small. Numerical simulations cannot hope to resolve all scales of motion present in real stellar convection and must instead strike a compromise between resolving dynamics on small scales and capturing the connectivity and geometry of the global scales. Here we focus on the latter by studying a full spherical shell of convection.

2.1. Anelastic MHD Formulation

Our tool for exploring MHD stellar convection is the anelastic spherical harmonic (ASH) code, which is described in detail in Clune et al. (1999). The implementation of magnetism is discussed in Brun et al. (2004). ASH solves the 3D MHD anelastic equations of motion in a rotating spherical shell using the pseudo-spectral method and runs efficiently on massively parallel architectures. We use the anelastic approximation to capture the effects of density stratification without having to resolve sound waves which have short periods (about 5 minutes) relative to the dynamical time scales of the global scale convection (weeks to months) or possible cycles of stellar activity (years to decades). This criteria effectively filters out the fast magneto-acoustic modes while retaining the slow modes and Alfvén waves. Under the anelastic approximation the thermodynamic fluctuating variables are linearized about their spherically symmetric and evolving mean state, with radially varying density $\bar{\rho}$, pressure \bar{P} , temperature \bar{T} and specific entropy \bar{S} . The fluctuations about this mean state are denoted as ρ , P , T and S . In the reference frame of the star, rotating at average rotation rate Ω_0 , the resulting MHD equations are:

$$\nabla \cdot (\bar{\rho}v) = 0, \quad (1)$$

$$\nabla \cdot B = 0, \quad (2)$$

$$\bar{\rho} \left[\frac{\partial v}{\partial t} + (v \cdot \nabla)v + 2\Omega_0 \times v \right] = -\nabla(\bar{P} + P) \quad (3)$$

$$+(\bar{\rho} + \rho)g + \frac{1}{4\pi} (\nabla \times B) \times B - \nabla \cdot \mathcal{D},$$

$$\frac{\partial B}{\partial t} = \nabla \times (v \times B) - \nabla \times (\eta \nabla \times B), \quad (4)$$

$$\begin{aligned} \bar{\rho} \bar{T} \left[\frac{\partial S}{\partial t} + v \cdot \nabla(\bar{S} + S) \right] = \\ \nabla \cdot \left[\kappa_r \bar{\rho} c_p \nabla(\bar{T} + T) + \kappa_0 \bar{\rho} \bar{T} \nabla \bar{S} + \kappa \bar{\rho} \bar{T} \nabla S \right] \\ + \frac{4\pi\eta}{c^2} j^2 + 2\bar{\rho}\nu \left[e_{ij}e_{ij} - \frac{1}{3}(\nabla \cdot v)^2 \right], \end{aligned} \quad (5)$$

where $v = (v_r, v_\theta, v_\phi)$ is the local velocity in the stellar reference frame, $B = (B_r, B_\theta, B_\phi)$ is the magnetic field, j is the vector current density, g is the gravitational acceleration, c_p is the specific heat at constant pressure, κ_r is the radiative diffusivity and \mathcal{D} is the viscous stress tensor, given by

$$\mathcal{D}_{ij} = -2\bar{\rho}\nu \left[e_{ij} - \frac{1}{3}(\nabla \cdot v)\delta_{ij} \right], \quad (6)$$

where e_{ij} is the strain rate tensor. Here ν , κ and η are the diffusivities for vorticity, entropy and magnetic field. We assume an ideal gas law

$$\bar{P} = \mathcal{R}\bar{\rho}\bar{T}, \quad (7)$$

where \mathcal{R} is the gas constant, and close this set of equations using the linearized relations for the thermodynamic fluctuations of

$$\frac{\rho}{\bar{\rho}} = \frac{P}{\bar{P}} - \frac{T}{\bar{T}} = \frac{P}{\gamma\bar{P}} - \frac{S}{c_p}. \quad (8)$$

The mean state thermodynamic variables that vary with radius are evolved with the fluctuations, thus allowing the convection to modify the entropy gradients which drive it.

The mass flux and the magnetic field are represented with a toroidal-poloidal decomposition as

$$\bar{\rho}v = \nabla \times \nabla \times (W\hat{r}) + \nabla \times (Z\hat{r}), \quad (9)$$

$$B = \nabla \times \nabla \times (\beta\hat{r}) + \nabla \times (\zeta\hat{r}), \quad (10)$$

with streamfunctions W and Z and magnetic potentials β and ζ . This approach ensures that both quantities remain divergence-free to machine precision throughout the simulation. The velocity, magnetic and thermodynamic variables are all expanded in spherical harmonics for their horizontal structure and in Chebyshev polynomials for their radial structure. The solution is time evolved with a second-order Adams-Bashforth/Crank-Nicolson technique.

ASH is a large-eddy simulation (LES) code, with subgrid-scale (SGS) treatments for scales of motion which fall below the spatial resolution in our simulations. We treat these scales with effective eddy diffusivities, ν , κ and η , which represent the transport of momentum, entropy and magnetic field by unresolved motions in the simulations. These simulations are based on the hydrodynamic studies reported in Brown et al. (2008), and as there ν , κ and η are taken for simplicity as functions of radius alone and proportional to $\bar{\rho}^{-1/2}$. This adopted SGS variation, as in Brun et al. (2004) and Browning et al. (2006), yields lower diffusivities near the bottom of the layer and thus higher Reynolds numbers. Acting on the mean entropy gradient is the eddy thermal diffusion κ_0 which is treated separately and occupies a narrow region in the upper convection zone. Its purpose is to transport entropy through the outer surface where radial convective motions vanish.

TABLE 1
 PARAMETERS FOR PRIMARY SIMULATIONS

Case	N_r, N_θ, N_ϕ	Ra	Ta	Re	Re'	Rm	Rm'	Ro	Roc	ν	η	Ω_0/Ω_\odot
D3	$96 \times 256 \times 512$	3.22×10^5	1.22×10^7	173	105	86	52	0.378	0.311	1.32	2.64	3
D5	$96 \times 256 \times 512$	1.05×10^6	6.70×10^7	273	133	136	66	0.273	0.241	0.940	1.88	5
H3	$96 \times 256 \times 512$	4.10×10^5	1.22×10^7	335	105	—	—	0.427	0.353	1.32	—	3
H5	$96 \times 256 \times 512$	1.27×10^6	6.70×10^7	576	141	—	—	0.303	0.268	0.940	—	5

NOTE. — Dynamo simulations at three and five times the solar rotation rate are cases D3 and D5, and their hydrodynamic (non-magnetic) companions are H3 and H5. All simulations have inner radius $r_{\text{bot}} = 5.0 \times 10^{10}$ cm and outer radius of $r_{\text{top}} = 6.72 \times 10^{10}$ cm, with $L = (r_{\text{top}} - r_{\text{bot}}) = 1.72 \times 10^{10}$ cm the thickness of the spherical shell. Evaluated at mid-depth are the Rayleigh number $\text{Ra} = (-\partial\rho/\partial S)(d\bar{S}/dr)gL^4/\rho\nu\kappa$, the Taylor number $\text{Ta} = 4\Omega_0^2 L^4/\nu^2$, the rms Reynolds number $\text{Re} = v_{\text{rms}}L/\nu$ and fluctuating Reynolds number $\text{Re}' = v'_{\text{rms}}L/\nu$, the magnetic Reynolds number $\text{Rm} = v_{\text{rms}}L/\eta$ and fluctuating magnetic Reynolds number $\text{Rm}' = v'_{\text{rms}}L/\eta$, the Rossby number $\text{Ro} = \omega/2S\Omega_0$, and the convective Rossby number $\text{Roc} = (\text{Ra}/\text{TaPr})^{1/2}$. Here the fluctuating velocity v' has the axisymmetric component removed: $v' = v - \langle v \rangle$, with angle brackets denoting an average in longitude. For all simulations, the Prandtl number $\text{Pr} = \nu/\kappa$ is 0.25 and the magnetic Prandtl number $\text{Pm} = \nu/\eta$ is 0.5. The viscous and magnetic diffusivity, ν and η , are quoted at mid-depth (in units of 10^{12} cm²s⁻¹). The rotation rate Ω_0 of each reference frame is in multiples of the solar rate $\Omega_\odot = 2.6 \times 10^{-6}$ rad s⁻¹ or 414 nHz. The viscous time scale at mid-depth $\tau_\nu = L^2/\nu$ is 3640 days for case D5 and the resistive time scale is 1820 days. Rotation periods at three and five times the solar rate are in turn 9.3 days and 5.6 days.

The boundary conditions imposed at the top and bottom of the convective unstable shell are:

1. Impenetrable top and bottom: $v_r = 0$,
2. Stress-free top and bottom:

$$(\partial/\partial r)(v_\theta/r) = (\partial/\partial r)(v_\phi/r) = 0,$$

3. Constant entropy gradient at top and bottom:

$$\partial(S + \bar{S})/\partial r = \text{const}, \quad (11)$$

4. Match to external potential field at top:

$$B = \nabla\Phi \quad \text{and} \quad \nabla^2\Phi = 0|_{r=r_{\text{top}}},$$

5. Perfect conductor at bottom:

$$B_r = (\partial/\partial r)(B_\theta/r) = (\partial/\partial r)(B_\phi/r) = 0.$$

2.2. Posing the Dynamo Problem

Our simulations are a simplified picture of the vastly turbulent stellar convection zones present in G-type stars. We take solar values for the input entropy flux, mass and radius, and explore simulations of two stars rotating at three and five times the current solar rotation rate. We focus here on the bulk of the convection zone, with our computational domain extending from $0.72R_\odot$ to $0.97R_\odot$, thus spanning 172 Mm in radius. The total density contrast across the shell is about 25. The reference or mean state of our thermodynamic variables is derived from a 1D solar structure model (Brun et al. 2002) and is continuously updated with the spherically symmetric components of the thermodynamic fluctuations as the simulations proceed. The reference state in all of these simulations is similar to that shown in Brown et al. (2008). We avoid regions near the stellar surface where hydrogen ionization and radiative losses drive intense convection (like granulation) on very small scales that we cannot resolve, and thus position the upper boundary slightly below this region. Our lower boundary is positioned near the base of the convection zone, thus omitting the stably stratified radiative interior and the shear layer at the base of the convection zone known as the tachocline.

As in our previous work (Brown et al. 2008), we conducted our simulations at three and five times the solar rate Ω_\odot on a path where the SGS diffusivities ν , κ and η decrease as $\Omega_0^{-2/3}$, in order to maintain vigorous convection as rotation attempts to constrain and quench the motions. The fundamental characteristics of our simulations and parameters definitions are summarized in Table 1.

The dynamo simulations were initiated from mature hydrodynamic progenitor cases which had been evolved for at least 5000 days at each rotation rate and were well equilibrated. The progenitors are very similar to the cases reported in Brown et al. (2008), but we chose a functional form for the SGS entropy diffusion κ_0 that is more confined to the upper 10% of the convection zone; the unresolved flux here does not vary with rotation rate. The effects of this are subtle, resulting primarily in slightly stronger latitudinal gradients of differential rotation and temperature in the uppermost regions of the shell. The patterns of convection are very similar, though slightly more complex near the top of the shell, and the Reynolds number remains high throughout the shell. These cases were well evolved and possess intricate convective patterns and solar-like differential rotation profiles, with fast zonal flow at the equator and slower flows at the poles.

To initiate our dynamo cases, a small seed dipole magnetic field was introduced and evolved via the induction equation. The energy in the magnetic fields is initially many orders of magnitude smaller than the energy contained in the convective motions, but these fields are amplified by shear and grow to become comparable in energy to the convective motions.

These dynamo simulations are computationally intensive, requiring both high resolutions to correctly represent the velocity fields and long time evolution to capture the equilibrated dynamo behavior, which may include cyclic variations on time scales of several years. The strong magnetic fields can produce rapidly moving Alfvén waves which seriously restrict the Courant-Friedrichs-Lewy (CFL) timestep limits in the upper portions of the convection zone. Case D3, rotating three times faster than the current Sun, has been evolved for over 7000 days (or over 2 million timesteps), and case D5, rotating five times faster than the Sun, has seen more than 17000 days of evolution (representing more than 10 million timesteps).

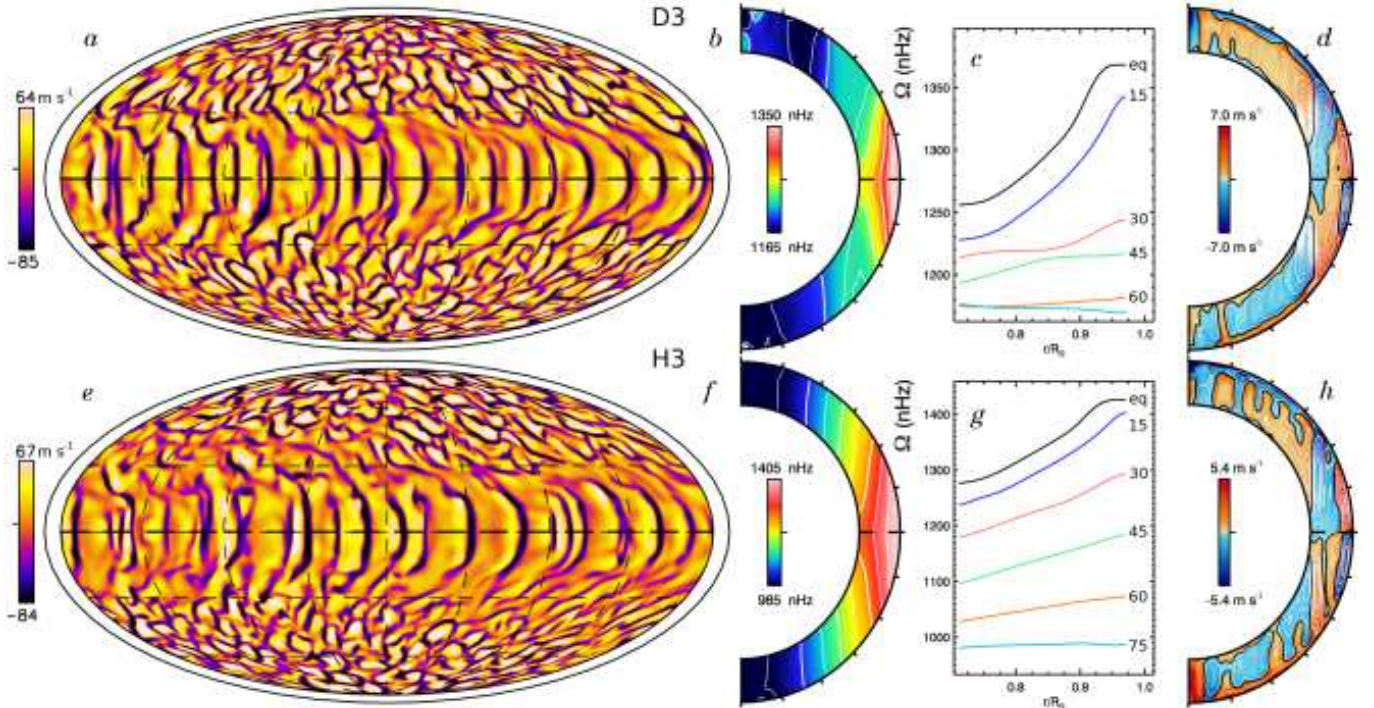


FIG. 1.— Convective structures and mean flows in cases D3 and H3. (a) Radial velocity v_r in dynamo case D3, shown in global Mollweide projection at $0.95R_\odot$, with upflows light and downflows dark. Poles are at top and bottom and the equator is the thick dashed line. The stellar surface at R_\odot is indicated by the thin surrounding line. (b) Profiles of mean angular velocity $\Omega(r, \theta)$, accompanied in (c) by radial cuts of Ω at selected latitudes. A strong differential rotation is established by the convection. (d) Profiles of meridional circulation, with sense of circulation indicated by color (red counter-clockwise, blue clockwise) and streamlines of mass flux overlaid. (e–h) Companion presentation of fields for hydrodynamic progenitor case H3. The patterns of radial velocity are very similar in both cases. The differential rotation is much stronger in the hydrodynamic case and the meridional circulations there are somewhat weaker, though their structure remains similar.

We plan to report on a variety of other dynamo cases, some at higher turbulence levels and rotation rates, in a subsequent paper.

These two cases were conducted at magnetic Prandtl number $Pm = \nu/\eta = 0.5$, a value significantly lower than employed in our previous solar simulations. In particular, Brun et al. (2004) explored $Pm = 2, 2.5$ and 4, and Browning et al. (2006) studied $Pm = 8$. The high magnetic Prandtl numbers were required in the solar simulations to reach sufficiently high magnetic Reynolds numbers to drive sustained dynamo action. In the simulations of Brun et al. (2004) only the simulations with $Pm > 2.5$ and $Rm' \gtrsim 300$ achieved sustained dynamo action, where Rm' is the fluctuating magnetic Reynolds number. We are here able to use a lower magnetic Prandtl number for three reasons. Firstly, more rapid rotation tends to stabilize convection and lower values of ν and η are required to drive the convection. Once convective motions begin however they become quite vigorous and the fluctuating velocities saturate at values comparable to our solar cases. Thus the Reynolds numbers achieved are fairly large and we can achieve modestly high magnetic Reynolds numbers even at low Pm . Secondly, the differential rotation becomes substantially stronger with both more rapid rotation Ω_0 and with lower diffusivities ν and η . This global-scale flow is an important ingredient and reservoir of energy for these dynamos, and the increase in its amplitude means that low Pm dynamos can still achieve large magnetic Reynolds numbers based on this zonal flow. Lastly, the critical magnetic Reynolds number for dynamo action likely decreases with increasing kinetic helicity (e.g., Leorat et al. 1981). Helicity generally increases with rotation rate (e.g., Käpylä et al. 2009), so the rapidly rotating flows considered here achieve dynamo action at somewhat lower

Rm than the models of Brun et al. (2004), which rotated at the solar rate.

3. DYNAMOS WITH PERSISTENT MAGNETIC WREATHES

We begin by turning to case D3 which yielded fairly persistent wreathes of magnetism in its two hemispheres, though these did wax and wane somewhat in strength once established. Examining the properties of this dynamo solution help to provide a perspective for the greater variations realized in our more rapidly rotating case D5.

3.1. Patterns of Convection

The complex and evolving convective structures in our dynamo cases are substantially similar to the patterns of convection found in our hydrodynamic simulations. Our dynamo solution rotating at three times the solar rate, case D3, is presented in Figure 1, along with its hydrodynamic progenitor, case H3. The radial velocities shown near the top of the simulated domain (Figs. 1a,e) have broad upflows and narrow downflows as a consequence of the compressible motions. Near the equator the convection is aligned largely in the north-south direction, and these broad fronts sweep through the domain in a prograde fashion. The strongest downflows penetrate to the bottom of the convection zone; the weaker flows are partially truncated by the strong zonal flows of differential rotation. In the polar regions the convection is more isotropic and cyclonic. There the networks of downflow lanes surround upflows and both propagate in a retrograde fashion.

The convection establishes a prominent differential rotation profile by redistributing angular momentum and entropy, building gradients in latitude of angular velocity and temperature. Figures 1b,f show the mean angular velocity $\Omega(r, \theta)$

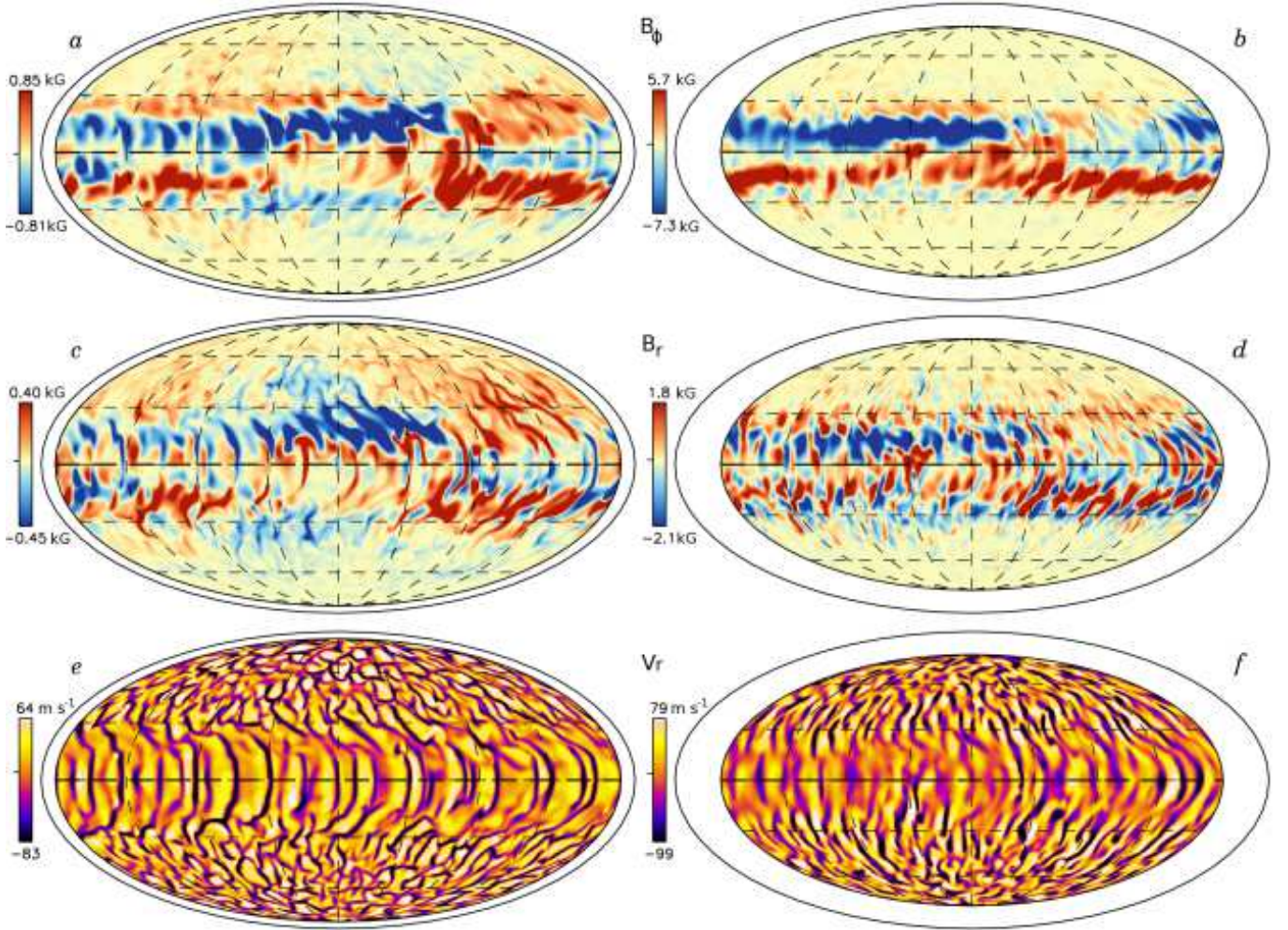


FIG. 2. — Magnetic wreathes and convective flows sampled at the same instant in case D3. (a) Longitudinal magnetic field B_ϕ near the top of the shell ($0.95R_\odot$) and (b) at mid-depth ($0.85R_\odot$). Strong flux structures with opposite polarity lie above and below the equator and span the convection zone. (c, d) Weaker radial magnetic field B_r permeates and encircles each wreath. (e, f) Strong convective upflows and downflows shown by V_r pass through and around the wreathes. The regions of strong magnetism tend to disrupt the convective flows while the strongest downflows serve to pump the wreathes to greater depths.

for cases D3 and H3, revealing a solar-like structure with a prograde (fast) equator and retrograde (slow) pole. This property is also realized for cases D5 and H5 with faster rotation. Figures 1c, g present in turn radial cuts of Ω at selected latitudes, which are useful as we consider the angular velocity patterns realized here with faster rotation. These $\Omega(r, \theta)$ profiles are averaged in azimuth (longitude) and time over a period of roughly 200 days. Contours of constant angular velocity are aligned nearly on cylinders, influenced by the Taylor-Proudman theorem.

In the Sun, helioseismology has revealed that the contours of angular velocity are aligned almost on radial lines rather than on cylinders. The tilt of Ω contours in the Sun may be due in part to the thermal structure of the solar tachocline, as first found in the mean-field models of Rempel (2005) and then in 3D simulations of global-scale convection by Miesch et al. (2006). In those computations, it was realized that introducing a weak latitudinal gradient of entropy at the base of the convection zone, consistent with a thermal wind balance in a tachocline of shear, can serve to tilt the Ω contours toward a more radial alignment without significantly changing either the overall Ω contrast with latitude or the convective patterns. We expect similar behavior here, but at present, observations of rapidly rotating stars only measure differential rotation at

the surface and do not offer constraints on either the existence of tachoclines in young suns or the nature of their internal differential rotation profiles. As such, we have neglected the possible tachoclines of penetration and shear entirely in these models and instead adopt the simplification of imposing a constant radial entropy gradient at the bottom of the convection zone.

The differential rotation achieved is stronger in our hydrodynamic case H3 than in our dynamo case D3. This can be quantified by measurements of the latitudinal angular velocity shear $\Delta\Omega_{\text{lat}}$. Here, as in Brown et al. (2008), we define $\Delta\Omega_{\text{lat}}$ as the shear near the surface between the equator and a high latitude, say $\pm 60^\circ$

$$\Delta\Omega_{\text{lat}} = \Omega_{\text{eq}} - \Omega_{60}, \quad (12)$$

and the radial shear $\Delta\Omega_r$ as the angular velocity shear between the surface and bottom of the convection zone near the equator

$$\Delta\Omega_r = \Omega_{0.97R_\odot} - \Omega_{0.72R_\odot}. \quad (13)$$

We further define the relative shear as $\Delta\Omega_{\text{lat}}/\Omega_{\text{eq}}$. In both definitions, we average the measurements of $\Delta\Omega$ in the northern and southern hemispheres, as the rotation profile is often slightly asymmetric about the equator. Case H3 achieves an absolute contrast $\Delta\Omega_{\text{lat}}$ of $2.22 \mu\text{ rad s}^{-1}$ (352 nHz) and a relative contrast of 0.247. The strong global-scale magnetic fields

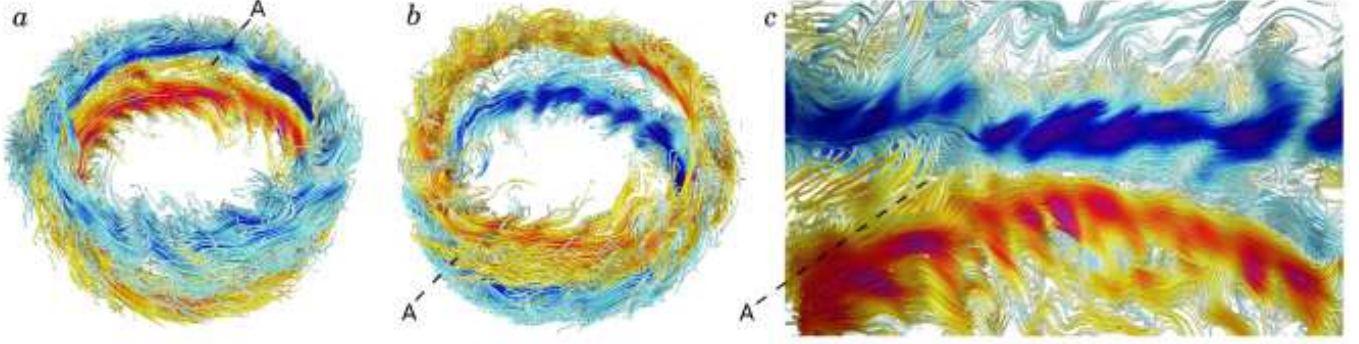


FIG. 3.— Field line tracings of magnetic wreathes in case D3. (a) Snapshot of two wreathes in full volume at same instant as in Fig. 2. Lines trace the magnetic fields, color denoting the amplitude and polarity of the longitudinal field B_ϕ (red, positive; blue, negative). Magnetic field threads in and out of the wreathes, connecting the two opposite polarity structures across the equator (i.e., region A) and to the polar regions where the magnetic field is wound up by the cyclonic convection. (b) Same snapshot showing south polar region. (c) Zoom in on region A showing the complex interconnections across the equator between the two wreathes and to high latitudes. Convective flows create the distinctive waviness visible in all three images.

TABLE 2
NEAR-SURFACE $\Delta\Omega$

Case	$\Delta\Omega_{\text{lat}}$	$\Delta\Omega_r$	$\Delta\Omega_{\text{lat}}/\Omega_{\text{eq}}$	Epoch
D3	1.17	0.71	0.136	6460-6920
D5 ^{avg}	1.14	0.71	0.083	3500-5700
D5 ^{min}	0.91	0.39	0.067	3702
D5 ^{max}	1.43	0.98	0.102	4060
H3	2.22	0.94	0.246	-
H5	2.77	1.31	0.192	-

NOTE. — Angular velocity shear in units of $\mu\text{rad s}^{-1}$, with $\Delta\Omega_{\text{lat}}$ and $\Delta\Omega_{\text{lat}}/\Omega_{\text{eq}}$ measured near the surface ($0.97R_\odot$) and $\Delta\Omega_r$ measured across the full shell at the equator. For the dynamo cases, these measurements are taken over the indicated range of days. In oscillating case D5, these measurements are averaged over a long epoch (*avg*), and are also taken at two instants in time when the differential rotation is particularly strong (*max*) and when magnetic fields have suppressed this flow (*min*). The hydrodynamic cases are each averaged for roughly 300 days. Case D3 also shows slow variations in $\Delta\Omega_{\text{lat}}$ over periods of about 2000 days.

realized in the dynamo case D3 serve to diminish the differential rotation. As such, this case achieves an absolute contrast $\Delta\Omega_{\text{lat}}$ of only $1.17 \mu\text{ rad s}^{-1}$ (186 nHz) and a relative contrast of 0.136. This results from both a slowing of the equatorial rotation rate and an increase in the rotation rate in the polar regions. These results are quoted in Table 2, along with related measurements for our five solar dynamo case D5 and hydrodynamic cases H3 and H5. It is interesting to note that in both dynamo cases the amount of latitudinal and radial shear is almost the same, whereas in the hydrodynamic simulations the more rapidly rotating case H5 has larger angular velocity contrasts than the slower case H3.

The meridional circulations realized in the dynamo case D3 are very similar to those found in its hydrodynamic progenitor (case H3). As illustrated in Figures 1d, h, the circulations are multi-celled in radius and latitude. The cells are strongly aligned with the rotation axis, though some flows along the inner and outer boundaries cross the tangent cylinder and serve to couple the polar regions to the equatorial convection. Flows of meridional circulation are slightly stronger in the dynamo cases than in the purely hydrodynamic cases, and these flows weaken with more rapid rotation.

3.2. Kinetic and Magnetic Energies

Convection in these rapidly rotating dynamos is responsible for building the differential rotation and the magnetic fields. In a volume averaged sense, the energy contained in the magnetic fields in case D3 is about 10% of the kinetic energy. About 35% of this kinetic energy is contained in the fluctuating convection (CKE) and about 65% in the differential rotation (DRKE), whereas the weaker meridional circulations contain only a small portion (MCKE). The magnetic energy is split between the contributions from fluctuating fields (FME), involving roughly 53% of the total magnetic energy, and the energy of the mean toroidal fields (TME) that are 43% of the total. The energy contained in the mean poloidal fields (PME) is only 4% of the total magnetic energy. These energies are defined as

$$\text{CKE} = \frac{1}{2}\bar{\rho} \left[(v_r - \langle v_r \rangle)^2 + (v_\theta - \langle v_\theta \rangle)^2 + (v_\phi - \langle v_\phi \rangle)^2 \right], \quad (14)$$

$$\text{DRKE} = \frac{1}{2}\bar{\rho} \langle v_\phi \rangle^2, \quad (15)$$

$$\text{MCKE} = \frac{1}{2}\bar{\rho} (\langle v_r \rangle^2 + \langle v_\theta \rangle^2), \quad (16)$$

$$\text{FME} = \frac{1}{8\pi} \left[(B_r - \langle B_r \rangle)^2 + (B_\theta - \langle B_\theta \rangle)^2 + (B_\phi - \langle B_\phi \rangle)^2 \right], \quad (17)$$

$$\text{TME} = \frac{1}{8\pi} \langle B_\phi \rangle^2, \quad (18)$$

$$\text{PME} = \frac{1}{8\pi} (\langle B_r \rangle^2 + \langle B_\theta \rangle^2). \quad (19)$$

where angle brackets denote an average in longitude.

These results are in contrast to our previous simulations of the solar dynamo, where the mean fields contained only about 2% of the magnetic energy and the fluctuating fields contained nearly 98% (Brun et al. 2004). In simulations of the solar dynamo that included a stable tachocline at the base of the convection zone (Browning et al. 2006), the energy of the mean fields in the tachocline can exceed the energy of the fluctuating fields there by about a factor of three, though the fluctuating fields still dominate the magnetic energy budget within the convection zone itself. Simulations of dynamo activity in the convecting cores of A-type stars (Brun et al. 2005) achieved similar results. There in the stable radiative zone the energies

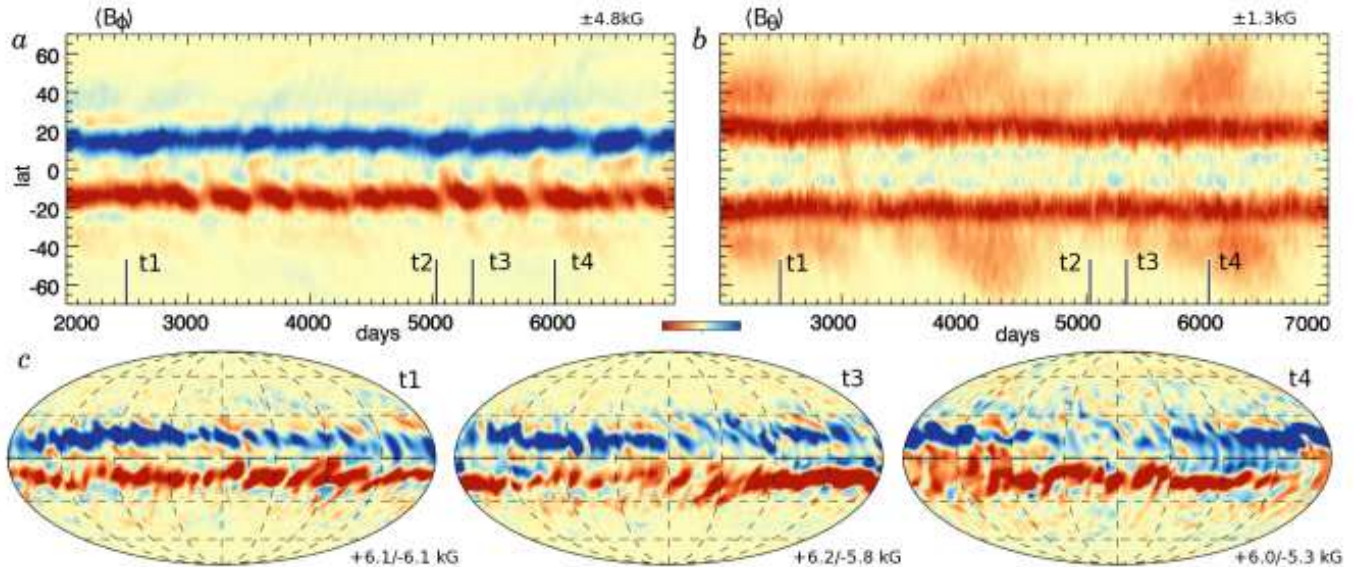


FIG. 4.— Persistent wreathes of magnetism in case D3. (a) Time-latitude plots of azimuthally-averaged longitudinal field $\langle B_\phi \rangle$ at mid-convection zone ($0.85R_\odot$) in a view spanning latitudes from $\pm 70^\circ$, with scaling values indicated. The two wreathes of opposite polarity persist for more than 4000 days. (b) Mean colatitudinal magnetic field $\langle B_\theta \rangle$ at mid-convection zone over same interval. (c) Snapshots of B_ϕ in Mollweide projection at mid-convection zone, shown for three times indicated in a, b. The wreathes maintain constant polarity over long time intervals, but still show variation as they interact with the convection. Time t2 corresponds to the snapshot in Fig. 2b.

TABLE 3
ENERGIES

Case	CKE	DRKE	MCKE	FME	TME	PME
D3	2.31	4.35	0.010	0.36	0.29	0.029
D5 ^{avg}	1.85	4.46	0.006	0.55	0.43	0.048
D5 ^{min}	1.70	2.85	0.005	0.50	0.25	0.062
D5 ^{max}	1.85	7.52	0.007	0.39	0.65	0.042
H3	2.56	22.2	0.012	-	-	-
H5	2.27	34.3	0.008	-	-	-

NOTE. — Volume-averaged energy densities relative to the rotating coordinate system. Kinetic energies are shown for convection (CKE), differential rotation (DRKE) and meridional circulations (MCKE). Magnetic energies are shown for fluctuating magnetic fields (FME), mean toroidal fields (TME) and mean poloidal fields (PME). All energy densities are reported in units of 10^6erg cm^{-3} and are averaged over 1000 day periods except for time-varying case D5, where intervals are as in Table 2.

of the mean fields were able to exceed the energy contained in the fluctuating fields, but in the convecting core the fluctuating fields contained roughly 95% of the magnetic energy. Simulations of dynamo action in fully-convective M-stars do however show high levels of magnetic energy in the mean fields (Browning 2008). In those simulations the fluctuating fields still contain much of the magnetic energy, but the mean toroidal fields possess about 18% of the total throughout most of the stellar interior. In our rapidly rotating suns, the mean fields comprise a significant portion of the magnetic energy in the convection zone and are as important as the fluctuating fields.

Convection is similarly strong in all four rapidly rotating cases, and CKE is similar in magnitude. The differential rotation in the dynamo cases is much weaker than in the hydrodynamic progenitors and DRKE has decreased by about a factor of five. The magnetic fields and differential rotation in case D5 change in time, but the average energy contained in DRKE is nearly the same in both dynamo cases despite their

very different rotation rates. This is in striking contrast to the behavior of the hydrodynamic cases, where DRKE is much larger in the more rapidly rotating case H5 than in case H3. Meridional circulations are comparably weak in all cases.

The amount of energy contained in the magnetic fields is different in these two dynamo cases, with energies generally stronger in case D5 than in case D3. In an average sense, all three magnetic energies are about 1.5 times greater in case D5 than in case D3. Case D5 shows substantial time variation, and at periods either FME or TME can become quite similar to those values realized in case D3. Meanwhile, PME is always stronger in D5 than in D3.

4. WREATHES OF MAGNETISM

These dynamos produce striking magnetic structures in the midst of their turbulent convection zones. The magnetic field is organized into large banded, wreath-like structures positioned near the equator and spanning the depth of the convection zone. These wreathes are shown at two depths in the convection zone in Figure 2. The dominant component of the magnetic wreathes is the strong longitudinal field B_ϕ , with each wreath possessing its own polarity. The average strength of the longitudinal field at mid-convection zone is $\pm 7 \text{ kG}$ and peak field strengths there reach roughly $\pm 26 \text{ kG}$. Threaded throughout the wreathes are weaker radial and latitudinal magnetic fields, which connect the two structures across the equator and also to the high-latitude regions.

These wreathes of magnetism survive despite being embedded in vigorous convective upflows and downflows. The convective flows leave their imprint on the magnetic structures, with individual downflow lanes entraining the magnetic field, advecting it away, and stretching it into B_r while leaving regions of locally reduced B_ϕ . The slower upflows carry stronger B_ϕ up from the depths. Where the magnetism is particularly strong the convective flows are disrupted. Meanwhile, where the convective flows are strongest, the longitudinal magnetic field is weakened and appears to vanish. In reality, the magnetic wreathes here are diving deeper below the mid-convection zone, apparently pumped down by the pum-

melting action of the strong downflows.

The deep structure of these wreathes is revealed by field line tracings throughout the volume, shown in Figure 3 for the same instant in time. The wreathes are topologically leaky structures, with magnetic field lines threading in and out of the surrounding convection. The wreathes are connected to the high-latitude (polar) convection, and on the poleward edges they show substantial winding from the highly vortical convection found there. This occurs in both the northern and southern hemispheres, as shown in two views at the same instant (north, Fig. 3a and south, Fig. 3b). It is here that the global-scale poloidal field is being regenerated by the coupling of fluctuating velocities and fluctuating fields. Magnetic fields cross the equator, tying the two wreathes together at many locations (Fig. 3c). The strongest convective downflows leave their imprint on the wreathes as regions where the field lines are dragged down deeper into the convection zone, yielding a wavy appearance to the wreathes as a whole.

4.1. Wreathes Persist for Long Epochs

The wreathes of magnetism built in case D3 persist for long periods of time, with little change in strength and no reversals in global-scale polarity for as long as we have pursued these calculations. The long-term stability of the wreathes realized by the dynamo of case D3 is shown in Figure 4. Here the azimuthally-averaged longitudinal field $\langle B_\phi \rangle$ and colatitudinal field $\langle B_\theta \rangle$ are shown at mid-convection zone at a point after the dynamo has equilibrated and for a period of roughly 5000 days (i.e., several ohmic diffusion times). During this interval there is little change in either the amplitude or structure of the mean fields. This is despite the short overturn times of the convection (10–30 days) or the rotation period of the star (~ 9 days). The ohmic diffusion time at mid-convection zone is approximately 1300 days.

Though the mean (global-scale) fields are roughly steady in nature (Figs. 4a,b), the magnetic field interacts strongly with the convection on smaller scales. Several samples of longitudinal field B_ϕ are shown in full Mollweide projection at mid-convection zone (Fig. 4c). The magnetic fields are clearly reacting on short time scales to the convection but the wreathes maintain their coherence.

There are also some small but repeated variations in the global-scale magnetic fields. Visible in Figure 4b are events where propagating structures of $\langle B_\theta \rangle$ reach toward higher latitudes over periods of about 1000 days (i.e., from day 3700 to day 4500 and from day 5600 to day 6400). These are accompanied by slight variations in the volume-averaged magnetic energy densities and the comparable kinetic energy of the differential rotation. These variations are also visible in the differential rotation itself, as shown in Figure 5. The differential rotation is fairly stable, though some time variation is visible at high latitudes. This is better revealed (Fig. 5b) by subtracting the time-averaged profile of Ω at each latitude, revealing the temporal variations about this mean. In the polar regions above $\pm 40^\circ$ latitude, speedup features move poleward over 500 day periods. These features track similar structures visible in the mean magnetic fields (Fig. 4b).

These evolving structures of magnetism and faster and slower differential rotation appear to be the first indications of behavior where the mean fields themselves begin to wax and wane substantially in strength. As the magnetic Reynolds number is increased, this time varying behavior becomes more prominent and can even result in organized changes in the global-scale polarity. Such behavior is evident in our

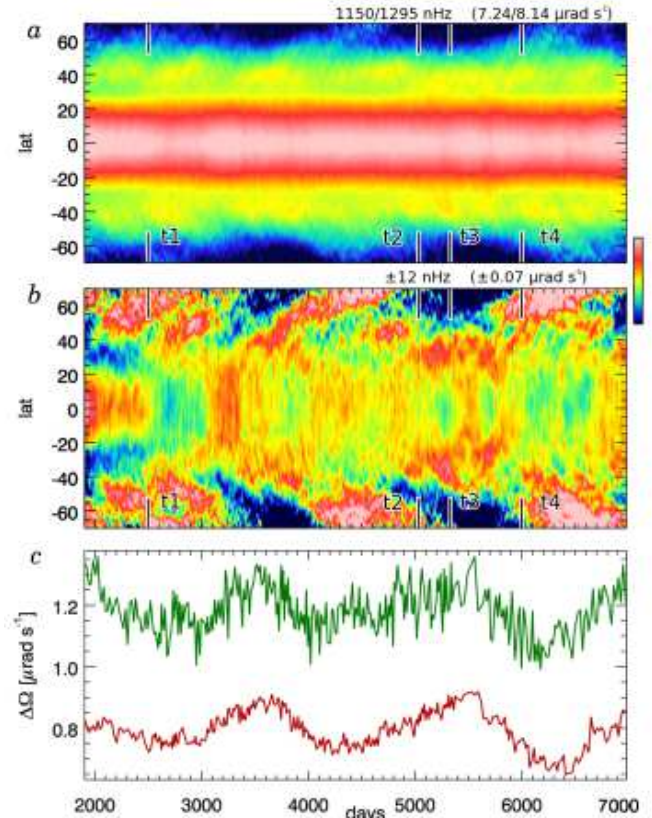


FIG. 5.— Differential rotation in case D3. (a) Angular velocity Ω at mid-convection zone ($0.85R_\odot$), with ranges in both nHz and $\mu\text{rad s}^{-1}$. The equator is fast while the poles rotate more slowly. (b) Temporal variations are emphasized by subtracting the time-averaged profile of $\Omega(r, \theta)$, revealing speedup structures at high latitudes and pulses of fast and slow motion near the equator. (c) Angular velocity shear $\Delta\Omega_{\text{lat}}$ (eq. 12) near the surface (upper curve, green) and at mid-convection zone (lower, red).

case D5.

5. A CYCLIC DYNAMO

Our more rapidly rotating simulation, case D5 at five times the current solar rate, also builds strong wreathes of magnetism that span the convection zone. In this simulation the dynamo is not steady in time and instead goes through cycles of activity. During a cycle, the global-scale magnetic fields wax and wane in strength and at the lowest field strengths they can flip their polarity. We shall begin by looking at the general properties of the convective flows and their associated differential rotation and meridional circulation, and then turn to examining the nature of the magnetic fields and their time-varying behavior.

5.1. Patterns of Convection in Case D5

Figure 6a shows a snapshot of the patterns of convection realized in case D5 near the top of the domain. Much as in the radial velocity patterns shown for case D3 (Figs. 1a,2e), here with faster rotation we continue to have prominent north-south aligned cells in the lower latitudes and more isotropic patterns near the poles. There is some modulation with longitude in the equatorial roll amplitudes. The downflows are fast and narrow, while the upflows are broader and slower. The convection establishes a prominent differential rotation, with a fast equator and slow poles (Fig. 6c).

As in case D3, here too the convective downflow structures propagate more rapidly than the differential rotation in which

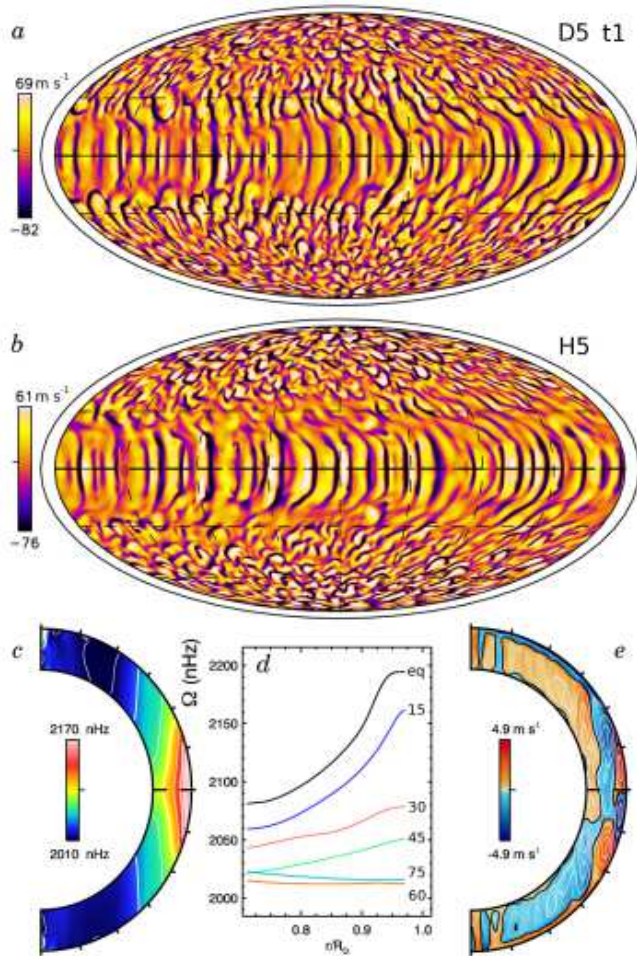


FIG. 6.— Patterns of convection at five times the solar rotation rate. (a) Radial velocity v_r in Mollweide projection at $0.95R_\odot$ for case D5. This snapshot samples day 3880 (time t1) when the magnetic fields are strong. (b) Companion hydrodynamic case H5, whose stronger differential rotation shears out convective structures in the mid-latitudes. (c) Profile of mean angular velocity $\Omega(r, \theta)$ for case D5, with (d) radial cuts of Ω at selected latitudes. (e) Meridional circulations for case D5, with magnitude and sense of circulation indicated by color (red counter-clockwise, blue clockwise) and streamlines of mass flux overlaid.

they are embedded. In the equatorial band, these structures move in a prograde fashion and at high latitudes in the retrograde sense. In the polar regions, the radial velocity patterns have a somewhat cuspy appearance, with the strongest downflows appearing to favor the westward and lower-latitude side of each convective cell. This may be a consequence of the strong retrograde differential rotation in those regions.

The convective structures are quite similar to those realized in the hydrodynamic case H5 (Fig. 6b), though there are some noticeable differences, particularly at the mid latitudes (around $\pm 30^\circ$). In the hydrodynamic case there is little radial flow in these regions, as the strong differential rotation shears out the convective cells. This region is equatorward of the tangent cylinder, an imaginary boundary tangent to the base of the convection zone and aligned with the rotation axis. For rotating convective shells, it has generally been found that the dynamics are different inside and outside the tangent cylinder, due to differences in connectivity and rotational constraint in these two regions (e.g., Busse 1970). The tangent cylinder in our geometry intersects with the stellar surface at roughly $\pm 42^\circ$ of latitude. In our compressible simulations, we generally find that the convective patterns in the equatorial regions

are bounded by a conic surface rather than the tangent cylinder (Brown et al. 2008). In case H5 the strong differential rotation serves to disrupt the convection at the mid-latitudes. In contrast, in the dynamo case D5 the differential rotation is substantially weaker in both radial and latitudinal angular velocity contrasts (Table 2). As is evident in Figure 6a, the convective cells fill in this region quite completely.

The time-averaged angular velocity profile $\Omega(r, \theta)$ is shown for case D5 in Figures 6c, d. The latitudinal angular velocity contrast $\Delta\Omega_{\text{lat}}$ and radial contrast $\Delta\Omega_r$ in this case is remarkably similar in amplitude to that realized in case D3 (Table 2), even though the basic rotation rate Ω_0 is substantially faster. This is in marked contrast to our hydrodynamic companion cases where faster rotation leads to greater angular velocity contrasts. The accompanying meridional circulation patterns for case D5 (Fig. 6e) appear to have three major cells of circulation in each hemisphere. These flows are weaker than in case D3. They are very similar to the circulations found in case H5.

5.2. Oscillations in Energies and Changes of Polarity

The dynamo action realized by the convection in case D5 exhibits significant changes in time. This time-varying behavior is readily visible as oscillations of the volume-averaged kinetic and magnetic energy densities, as shown in Figure 7a at a time long after the dynamo has saturated and reached equilibration. Here the kinetic energy of differential rotation (DRKE) undergoes factor of five changes on periods of 500-1000 days. As DRKE decreases the magnetic energies increase. Moving in concert are the mean toroidal (TME) and mean poloidal (PME) magnetic energies. The mean poloidal fields appear to lag slightly behind the mean toroidal fields as they both change in strength. The fluctuating magnetic energies (FME) track the largest rises in the mean fields but decouple during many of the deepest dips. In contrast, the variations in convective kinetic energies (CKE) show little organized behavior in time, and appear to change substantially only when the differential rotation is highly suppressed during the period from day 7500 to day 8300. The energy contained in the meridional circulations (MCKE) is weaker and not shown. Though it varies somewhat in time, there is not a clear relation to the changes in magnetic energies.

Magnetic energies in case D5 can rise to be a substantial fraction of the kinetic energies. Averaged over the nearly 16000 days shown here, the magnetic energies are about 17% of the kinetic energies. During individual oscillations the magnetic energies can range from a few percent of kinetic energies to levels as high as 50%. The kinetic energy is largely in the fluctuating convection and differential rotation, with CKE fairly constant and ranging from 15-60% of the total kinetic energy as DRKE grows and subsides, itself contributing between 40 to 85% of the kinetic energy. The magnetic energies are largely split between the mean toroidal fields and the fluctuating fields, with TME containing about 35% of the magnetic energy on average, FME containing about 61% and PME containing 4%. The roles of these energy reservoirs change somewhat through each oscillation. At any one time, between 10 and 60% of the magnetic energy is in TME while FME contains between 30 and 85% of the total. Meanwhile, PME can comprise as little as 1% or as much as 10% of the total. Generally, PME is about 12% of TME, but because PME lags the changes in TME slightly, there are periods of time when PME is almost 40% of TME.

The global-scale magnetic fields can reverse their polarities

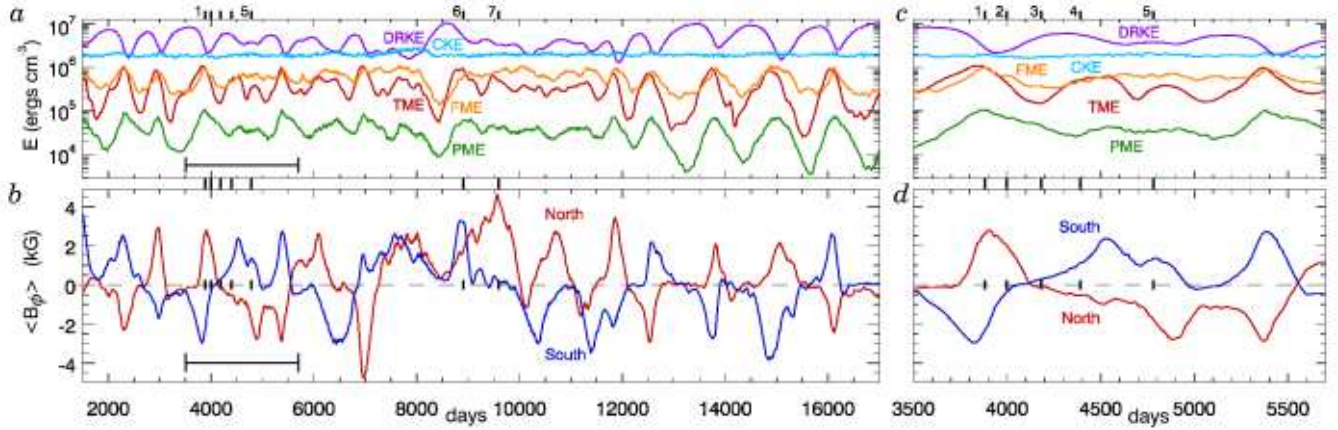


FIG. 7.— Complex time evolution in case D5 with flips in polarity of magnetic wreathes. (a) Volume-averaged energy densities for kinetic energy of convection (CKE), differential rotation (DRKE) and for magnetic energy in fluctuating fields (FME), in mean toroidal fields (TME) and in mean poloidal fields (PME) as labeled. Oscillations on roughly 500-1000 day periods are visible in the magnetic energies and in DRKE, though CKE stays nearly constant. (b) Mean toroidal field $\langle B_\phi \rangle$ averaged over entire northern and southern hemispheres (labeled) at mid-convection zone ($0.85R_\odot$). Early in the simulation, opposite polarities dominate each hemisphere. Several reversals occur, along with several extreme excursions which do not flip the polarity of the global-scale field. During the interval from roughly day 7700 to 10200, the dynamo falls into peculiar single polarity states, with one polarity dominating both hemispheres. Bracketed interval from day 3500 to 5700 spans one full polarity reversal; (c) shows volume-averaged energy densities during this period, and (d) the mean toroidal field. Thick labeled tick marks above *a, c* indicate time samples used in later images.

during some of the oscillations in magnetic energies. This is evident in Figure 7b showing averages at mid-convection zone of the longitudinal magnetic field $\langle B_\phi \rangle$ over the northern and southern hemispheres. Reversals in field polarity occur periodically, with typical time scales of roughly 1500 days. These reversals appear to happen shortly after peak magnetic energies are achieved, but do not occur every time magnetic energies undergo a full oscillation. Rather, it appears that several failed reversals occur where the magnetic energies drop and the average fields decline in strength, only to return with the same polarity a few hundred days later, for each successful polarity reversal.

We focus in the following discussion on one such reversal, shown in closeup in Figures 7c, d and spanning the interval of time between days 3500 and 5700. Two reversals occur during this interval, with the global polarities flipping into a new state at roughly day 4100 and then changing back again at about day 5500. Detailed measurements of kinetic and magnetic energies during this interval are shown in Table 3.

5.3. Global-Scale Magnetic Reversals

The nature of the global-scale magnetic fields during the reversal spanning days 3500-5700 are presented in detail in Figure 8. Several samples of longitudinal magnetic field B_ϕ are shown at mid-convection zone spanning this time period. The timing of these samples is indicated in Figure 7 by numeric labels and likewise in Figure 8a which shows azimuthally-averaged $\langle B_\phi \rangle$ in a time-latitude map that spans the reversal.

Before a reversal, the magnetic wreathes of case D5 are very similar in appearance to the wreathes realized in case D3. They are dominated by the azimuthally-averaged component of B_ϕ , while also showing small-scale variations where convective plumes distort the fields (Fig. 8b). At mid-convection zone, typical longitudinal field strengths are of order ± 13 kG, while peak field strengths there can reach ± 40 kG. Meanwhile $\langle B_\phi \rangle$ is fairly anti-symmetric between the northern and southern hemispheres (Fig. 8g). Shortly before a reversal, the magnetic wreathes strengthen in amplitude and become more anti-symmetric about the equator.

They reach their peak values just before the polarity change at roughly day 4000 but then quickly begin to unravel, gain-

ing significant structure on smaller scales (Fig. 8c). At the same time, prominent magnetic structures detach from the higher-latitude edges and begin migrating toward the polar regions. Meanwhile, $\langle B_\phi \rangle$ loses its anti-symmetry between the two hemispheres, with $\langle B_\phi \rangle$ in one hemisphere typically remaining stronger and more concentrated than in the other (Fig. 8h). The stronger hemisphere (here the northern) retains its polarity for about 100 days as the fields in the other hemisphere (here southern) weaken and reverse in polarity. At this point the new wreathes of the next cycle, with opposite polarity, are already faintly visible at the equator.

Within 100 days these new wreathes grow in strength and become comparable with the structures they replace, which are still visible at higher latitudes (Figs. 8d, i). The mean $\langle B_\phi \rangle$ begins to contribute significantly to the overall structure of the new wreathes, and soon the polarity reversal is completed. In the interval immediately after the reversal, small-scale fluctuations still contribute significantly to the overall structure of the wreathes, and B_ϕ has complicated structure at mid-convection zone. At this time, the peak magnetic field strengths are somewhat lower, at about ± 20 kG. As $\langle B_\phi \rangle$ becomes stronger, the wreathes return to an anti-symmetric state, with similar amplitudes and structure in both the northern and southern hemispheres (Figs. 8e, j). They look much as they did before the reversal, though now with opposite polarities.

The wreathes from the previous cycle appear to move through the lower convection zone and toward higher latitudes. This can be seen variously in the time-latitude map at mid-convection zone (Fig. 8a), in the Mollweide snapshots (Figs. 8c–e) as well as in the samples of $\langle B_\phi \rangle$ (Figs. 8h–j). This poleward migration is likely due to hoop stresses within the magnetic wreathes and an associated poleward-slip instability (e.g., Spruit & van Ballegoijen 1982; Moreno-Insertis et al. 1992). Even at late times some signatures of the previous wreathes persist in the polar regions, and are still visible in Figures 8e, j at day 4390. They are much weaker in amplitude than the wreathes at the equator, but they persist until the wreathes from the next cycle move poleward and replace them. As they approach the polar regions, the old wreathes dissipate on both large and small

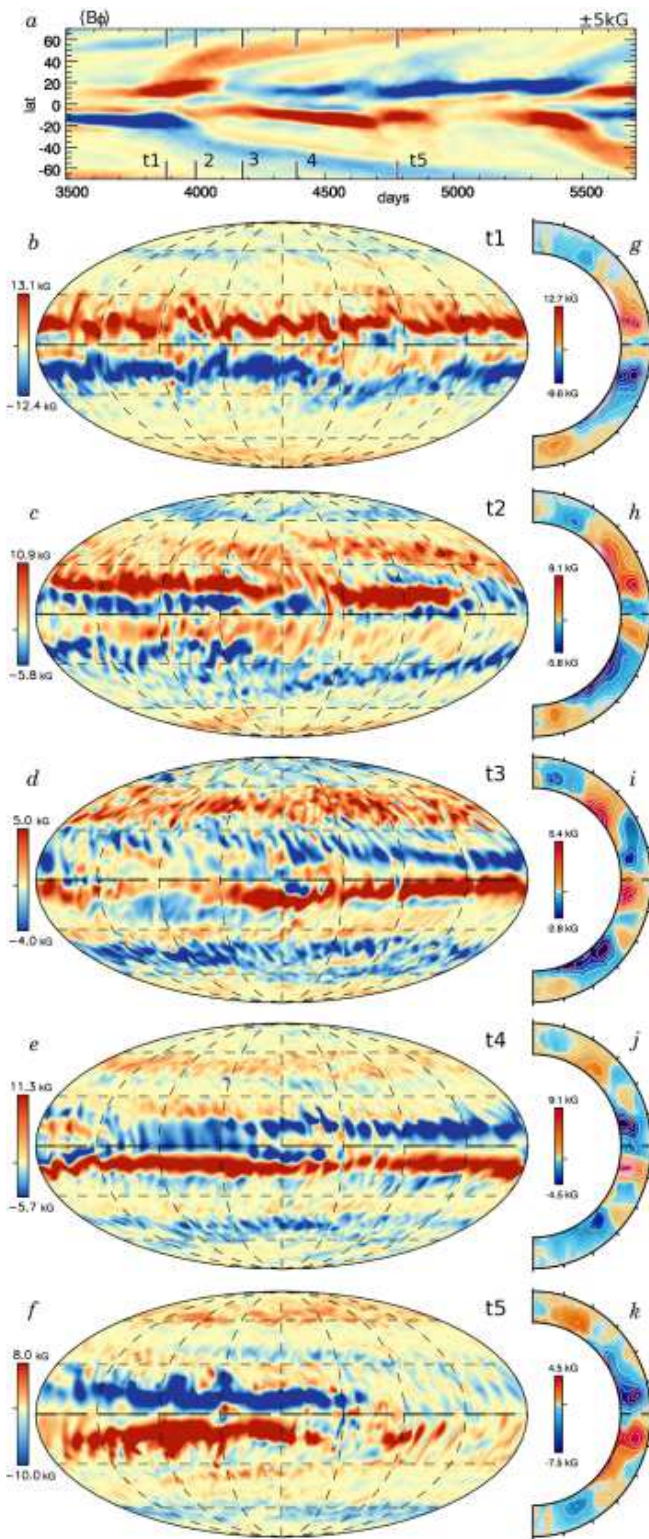


FIG. 8.— Evolution of longitudinal magnetic fields during a polarity reversal. (a) Time-latitude plot of $\langle B_\phi \rangle$ at mid-convection zone. (b–f) Snapshots of B_ϕ in Mollweide projection at mid-convection zone ($0.85R_\odot$) at times indicated by numbers in a. Between reversals the field is dominated by the mean component, but during reversals substantial fluctuations develop. (g–k) Accompanying samples of azimuthally-averaged $\langle B_\phi \rangle$, showing structure of mean fields with radius and latitude at same instants in time.

scales, for the vortical polar convection shreds them apart and ohmic diffusion reconnects them with the relic wreathes of the previous cycle.

Though reversals occur on average once every 1500 days, substantial variations can occur on shorter time scales. Here at mid-cycle the mean longitudinal field $\langle B_\phi \rangle$ becomes quite weak as the wreathes become concentrated in smaller longitudinal intervals of the equatorial region (as in Figs. 8f, k at day 4780). At other times the mean longitudinal fields become quite asymmetric, with one hemisphere strong and one weak (i.e., during days 4900–5200) before regaining their anti-symmetric nature shortly prior to the next reversal.

5.4. Temporal Changes in Differential Rotation

The strong magnetic fields in case D5 suppress the global-scale flow of differential rotation. As the fields themselves vary in strength, the differential rotation responds in turn, becoming stronger as the fields weaken and then diminishing as the fields are amplified. These cycles of faster and slower differential rotation are visible in the traces of DRKE shown in Figure 7a. We revisit here the interval explored in closer detail both in Figure 7c and in Figure 8, spanning days 3500 to 5700 of the simulation and one full polarity reversal.

The angular velocity Ω at mid-convection zone is shown for this period as a time-latitude map in Figure 9a. Here again the timing marks t1–t5 refer to the snapshots of B_ϕ shown in Figures 8b–k. In the equatorial regions, the differential rotation remains fast and prograde, but with some modulation in time. Prominent structures of speedup are visible propagating toward the poles at the high latitudes. These structures are much more evident when we subtract the time-averaged profile of Ω for this period at each latitude (Fig. 9b). They appear as strong, tilted fast (red) structures extending from roughly $\pm 30^\circ$ latitude poleward. In the northern hemisphere, three such structures are launched over this interval. In contrast, in the south only two such structures are evident. One is perhaps launched around day 4500 but does not survive or propagate. Comparing these features with the propagation of magnetic fields shown in Figure 8a over the same interval, we find that velocity speedup features are well correlated with the poleward migration of mean longitudinal magnetic field. The velocity features bear some resemblance to the poleward branch of torsional oscillations observed in the solar convection zone over the course of a solar magnetic activity cycle, though on a much shorter time scale here as befits the correspondingly shorter time between magnetic polarity reversals in these dynamo simulations.

These velocity features propagate toward the poles relatively slowly. In a period of roughly 500 days they travel about 40° in latitude, or a distance of about 410 Mm. Their propagation velocity is about 0.8 Mm day^{-1} or about 9 ms^{-1} . This is considerably slower than the fluctuating latitudinal flows associated with the convection which at this depth have peak speeds of $\pm 200 \text{ ms}^{-1}$ during this time period. The meridional circulations have amplitudes of about $\pm 6 \text{ ms}^{-1}$ here but do not have a latitudinal structure at all similar to the pattern propagation. The propagation speed of the speedup patterns is closer to the Alfvén velocity of the mean latitudinal magnetic fields, namely

$$v_{A,\theta} = \frac{\langle B_\theta \rangle}{\sqrt{4\pi\rho}}. \quad (20)$$

At mid-convection zone the mean density is about 0.065 g cm^{-3} and $\langle B_\theta \rangle$ in the poleward propagating plumes

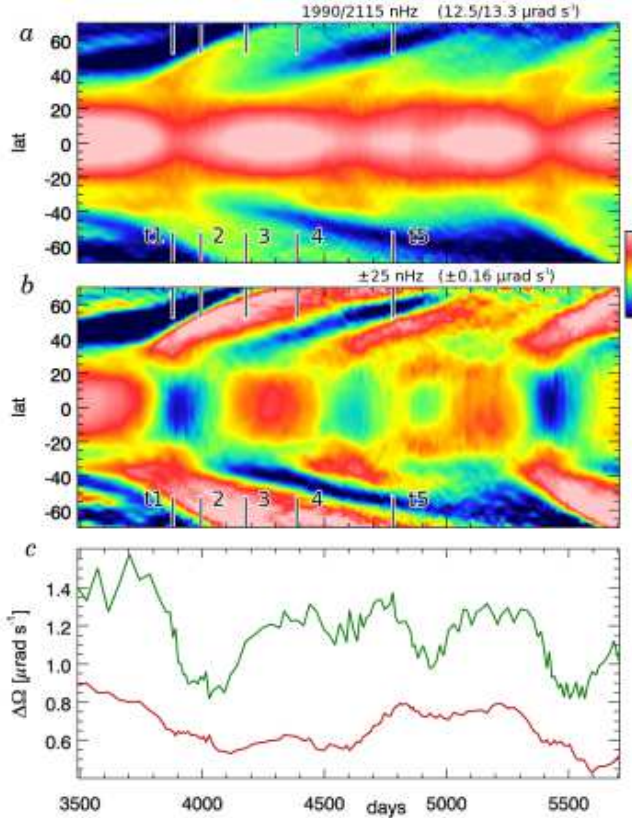


FIG. 9.— Time-varying differential rotation in case D5. (a) Time-latitude map of angular velocity Ω at mid-convection zone ($0.85R_{\odot}$). There are substantial temporal variations at both the equator and high latitudes. (b) These are accentuated by subtracting the time-averaged profile of $\Omega(r, \theta)$ at each latitude. Visible are poleward propagating speedup structures at high latitudes and more uniform modulations near the equator. (c) Corresponding variations in $\Delta\Omega_{\text{lat}}$ near the surface (upper curve, green) and at mid-convection zone (lower, red).

ranges between roughly ± 1.5 kG, yielding Alfvén velocities of about ± 17 ms^{-1} . This poleward migration may also be due to a poleward-slip instability arising from the strong toroidal fields. In this scenario, if we neglect rotation and turbulent pumping in latitude (e.g., Moreno-Insertis et al. 1992; Jouve & Brun 2009), the propagation speed should be approximately the Alfvén velocity of the mean toroidal magnetic fields, or about ± 45 ms^{-1} based on a mid-convection zone B_{ϕ} of approximately ± 4 kG in the propagating features. If the poleward-slip instability is occurring, the velocity speedup features may result from conservation of angular momentum in the plasma that travels poleward with the wreathes. Rotation is likely to partially stabilize wreathes against poleward-slip (Moreno-Insertis et al. 1992), and this may help explain their slower poleward propagation. The leaky topology of the wreathes will allow plasma to escape these structures, and this may modify the rate of their poleward propagation. The weak propagating features seen in case D3 (Fig. 5) required nearly 700 days to propagate a similar distance in latitude. This difference may be due to the somewhat lower magnetic field strengths achieved in that dynamo.

With the expanded sensitivity of Figure 9b, we can see that the equatorial modulation appears as fast and slow pulses which span the latitude range of $\pm 20^{\circ}$. These variations are fairly uniform across this equatorial region. The velocity variations at the equator do not correspond with the equatorial propagating branch of torsional oscillations seen in the Sun

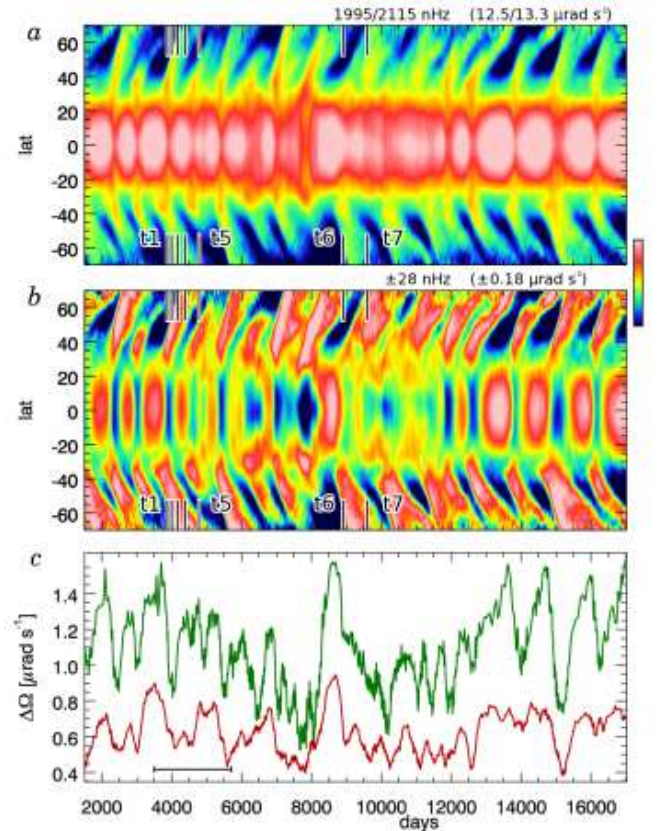


FIG. 10.— Extended history of temporally-varying differential rotation in Case D5. (a) Variations of $\Omega(r, \theta)$ at mid-convection zone. (b) Temporal variations are emphasized by subtracting the time-averaged profile of Ω . Poleward propagating speedup structures are visible in each magnetic oscillation. (c) Variations in $\Delta\Omega_{\text{lat}}$ near the surface (upper curve, green) and at mid-convection zone (lower, red).

(Thompson et al. 2003). In the Sun, the equatorial branch may arise from enhanced cooling in the magnetically active regions (e.g., Spruit 2003; Rempel 2006, 2007).

The temporal variations of the angular velocity contrast in latitude $\Delta\Omega_{\text{lat}}$ is shown for this period in Figure 9c. At mid-convection zone (sampled by red line) the variations in $\Delta\Omega_{\text{lat}}$ are modest, varying by roughly 15%. Near the surface (green line) $\Delta\Omega_{\text{lat}}$ shows more substantial variations, with large contrasts when the fields are strong in the magnetic cycle (prior to t1) and smaller contrasts when the fields are in the process of reversing (t2, t3). These near-surface values of $\Delta\Omega_{\text{lat}}$ are reported in Table 2, averaged over this entire period (avg) and at points in time when the contrast is large (max, at day 3702) and small (min, at day 4060).

6. SAMPLING MANY MAGNETIC CYCLES IN CASE D5

The variations of angular velocities over considerably longer intervals of time for case D5 are shown in Figures 10a,b. Here too we see the equatorial modulation over many magnetic cycles and the poleward propagating speedup bands. Asymmetries between the northern and southern hemisphere are evident at many times in different cycles. The latitudinal angular velocity contrasts shown in Figure 10c exhibit large variations. Successive magnetic cycles can have distinctly different angular velocity contrasts, and there are additional long-term modulations that span many magnetic cycles.

A sampling of the associated magnetic field behavior is shown in the time-latitude maps of $\langle B_{\phi} \rangle$ and $\langle B_{\theta} \rangle$ in Figures 11a,b. From day 1500 to 7300, four cycles occur in

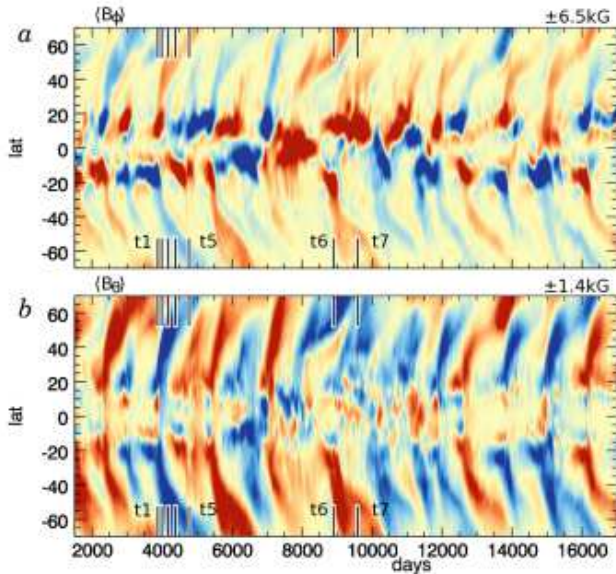


FIG. 11.— Time-latitude plots for case D5. Shown at mid-convection zone are (a) mean longitudinal field $\langle B_\phi \rangle$, and (b) mean colatitudinal field $\langle B_\theta \rangle$. Cycles of activity are visible, with fields changing polarity in the equatorial region. Also prominently visible are plumes of field reaching toward the polar regions in a manner recalling Fig. 4. The time samples used in Figs. 8 and 12 are indicated.

which wreathes of opposite polarity are achieved in each hemisphere. After this period, the dynamo explores unusual single-polarity states. Here either a single wreath is built (t7), or two wreathes of the same polarity (t6) occupy the two hemispheres. After day 10700 the dynamo emerges from this state and returns to building two wreathes of opposite polarity which flip in their sense an additional three times as the simulation continues.

The poleward propagating magnetic features shown previously in Figures 8a are evident throughout this longer time sampling, now appearing as nearly vertical streaks in both $\langle B_\phi \rangle$ and $\langle B_\theta \rangle$. These features continue to correlate well with the velocity speedup features evident in Figure 10b.

6.1. Strange States and Wreathes of a Single Polarity

These oscillating dynamos occasionally wander into distinctly different states, and this occurs for case D5 around day 7300. Instead of the two nearly anti-symmetric wreathes of opposite polarity above and below the equator, the dynamo enters a state where the polarity in each hemisphere is the same, as shown in Figures 12a,b at day 8903. Here two wreathes of same polarity occupy the two hemispheres and persist for an interval of more than 500 days. The positive-polarity B_ϕ reaches average amplitudes of 18 kG while the negative polarity structures have average amplitudes around 3 kG. The azimuthally-averaged profiles of $\langle B_\phi \rangle$ emphasize that these wreathes span the convection zone and have the same polarity everywhere. During this interval of time, the mean poloidal field has changed from the odd- ℓ components, to an even-parity state where the even- ℓ components are more prominent.

The dynamo can also achieve states where only a single wreath is built in the equatorial regions, as in Figures 12c,d at day 9590. Here a single strong wreath of positive polarity fills the northern hemisphere, with $\langle B_\phi \rangle$ reaching a peak amplitude of +18 kG. This unique structure persists for about 800 days before the dynamo flips polarity and builds a strong wreath

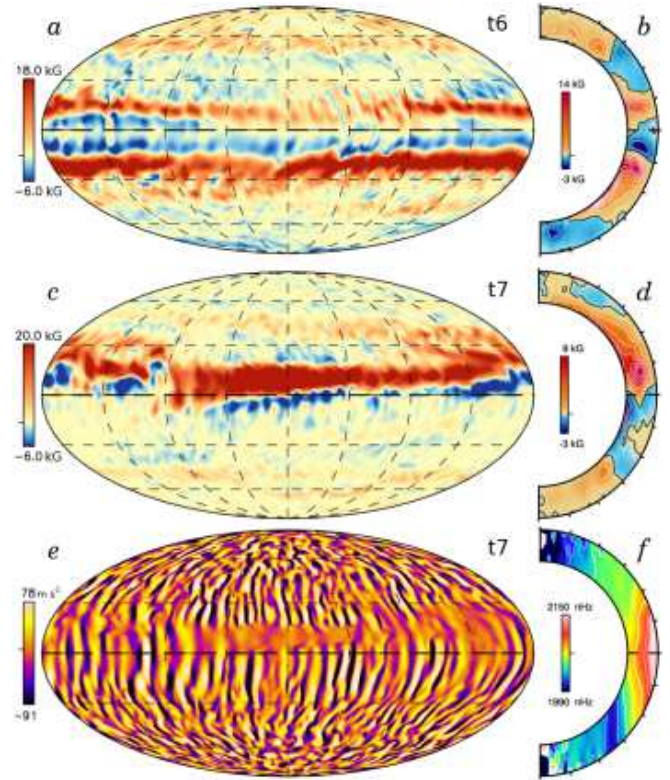


FIG. 12.— Strange states in case D5. (a) Snapshot of B_ϕ at mid-convection zone, showing two strong wreathes of the same polarity. (b) Instantaneous profile of $\langle B_\phi \rangle$ at same time. (c) Snapshot of B_ϕ at mid-convection zone at a time when a single wreath is formed. (d) Weaker negative polarity structures are visible in profile of $\langle B_\phi \rangle$ at same instant. (e) Accompanying snapshot of v_r at mid-convection zone, showing flows strongly affected by magnetism. (f) The instantaneous differential rotation, shown here as profile of $\Omega(r, \theta)$, is unaffected by the strong wreath.

of negative polarity. The predecessor of this new wreath can be seen in profiles of $\langle B_\phi \rangle$ where a much weaker structure of negative polarity is visible in the lower convection zone.

The strong magnetic fields realized in the single wreath states react back on the convective flows. This is evident in the accompanying snapshot of radial velocities at mid-convection zone (Fig. 12e). In a narrow band spanning $0-20^\circ$ latitude and coinciding with the strong tube, the upflows and downflows have been virtually erased. Fluctuations in v_ϕ and v_θ are also very small in this region, and the flow is dominated by the streaming flows of differential rotation. Within the wreath the total magnetic energy (ME) at mid-convection zone is locally about 10 to 100 times larger than the total kinetic energy (KE), while outside the wreath KE exceeds ME by factors of roughly 10 to 10^4 at this depth. We see similar restriction of the convective flows whenever the magnetic fields become this strong.

The differential rotation itself (Fig. 12f) is largely unaffected by the presence of the strong magnetic wreath. There is no clear signature of faster flow down the middle of the wreath. Likewise, there is no sign of the structure in profiles of the thermodynamic variables P, T, S , or ρ , with the mean profile instead dominated by latitudinal variations consistent with thermal wind balance.

7. CREATING MAGNETIC WREATHES

The magnetic wreathes formed in case D3 are dominated by strong mean longitudinal field components and show lit-

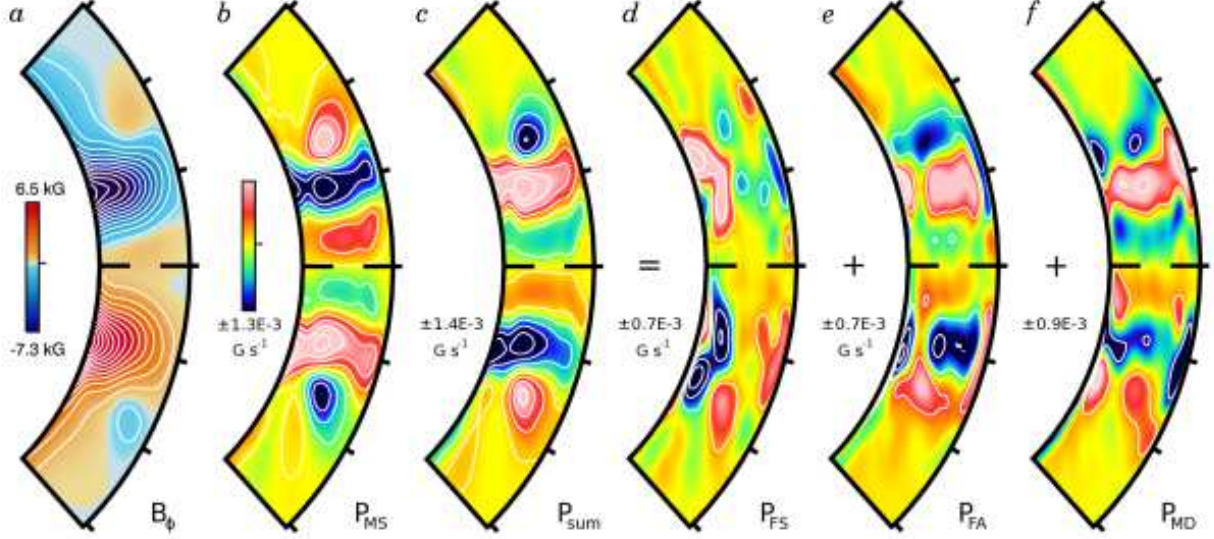


FIG. 13.— Generation of mean toroidal magnetic field in case D3. The view is from $\pm 45^\circ$ latitude to emphasize the equatorial regions. (a) Mean toroidal field $\langle B_\phi \rangle$ with wreathes strongly evident. (b) Production by P_{MS} serves to build $\langle B_\phi \rangle$. This rate term generally matches the sense of $\langle B_\phi \rangle$, thus being negative (blue in colorbar, with ranges indicated) in the core of the northern wreath and positive (red) in that of the southern wreath. (c) Destruction of mean toroidal field is achieved by the sum of the two fluctuating (turbulent) induction terms and the ohmic diffusion ($P_{FS} + P_{FA} + P_{MD}$). This sum clearly has opposite sense and similar magnitude to P_{MS} . We break out these three destruction terms in the following panels. (d) Fluctuating (turbulent) shear P_{FS} is strongest near the high-latitude side of each wreath, and (e) fluctuating (turbulent) advection P_{FA} is strongest in the cores of the wreathes. The sum of these terms ($P_{FS} + P_{FA}$) is responsible for about half the destructive balance, with the remainder coming from (f) the mean ohmic diffusion P_{MD} . Some differences arise in the boundary layers at top and bottom.

tle variation in time. To understand the physical processes responsible for maintaining these magnetic wreathes, we examine the terms arising in the time- and azimuth-averaged induction equation for case D3.

7.1. Maintaining Wreathes of Toroidal Field

We begin our analysis by exploring the maintenance of the mean toroidal field $\langle B_\phi \rangle$. Here it is helpful to break the induction term from equation (4) into contributions from shear, advection and compression, namely

$$\nabla \times (v \times B) = \underbrace{(B \cdot \nabla)v}_{\text{shear}} - \underbrace{(v \cdot \nabla)B}_{\text{advection}} - \underbrace{B(\nabla \cdot v)}_{\text{compression}}. \quad (21)$$

Details of this decomposition are given in the Appendix.

The evolution of the mean longitudinal (toroidal) field $\langle B_\phi \rangle$ is described symbolically in equation (A8), with individual terms defined in equation (A9). When we analyze these terms in case D3, we find that $\langle B_\phi \rangle$ is produced by the shear of differential rotation and is dissipated by a combination of turbulent induction and ohmic diffusion. This balance can be restated as

$$\frac{\partial \langle B_\phi \rangle}{\partial t} \approx P_{MS} + (P_{FS} + P_{FA} + P_{MD}) \approx 0, \quad (22)$$

with P_{MS} representing production by the mean shearing flow of differential rotation, P_{FS} by fluctuating shear, P_{FA} by fluctuating advection, and P_{MD} by mean ohmic diffusion. Those terms are in turn

$$P_{MS} = \langle (B \cdot \nabla) \langle v \rangle \rangle_\phi, \quad (23)$$

$$P_{FS} = \langle (B' \cdot \nabla) v' \rangle_\phi, \quad (24)$$

$$P_{FA} = -\langle (v' \cdot \nabla) B' \rangle_\phi, \quad (25)$$

$$P_{MD} = -\nabla \times \eta \nabla \times \langle B \rangle_\phi, \quad (26)$$

where brackets again indicate an azimuthal average and primes indicate fluctuating terms: $v' = v - \langle v \rangle$. The detailed implementation of these terms is presented for our spherical geometry in equations (A10-A15). These terms are illustrated in Figure 13 for case D3, averaged over a 450 day interval from day 6450 to 6900.

The structure of $\langle B_\phi \rangle$ is shown in Figure 13a. The shearing flows of differential rotation P_{MS} (Fig. 13b) act almost everywhere to reinforce the mean toroidal field. Thus the polarity of this production term generally matches that of $\langle B_\phi \rangle$. This production is balanced by destruction of mean field arising from both turbulent induction and ohmic diffusion (sum shown in Fig. 13c). The individual profiles of P_{FS} , P_{FA} and P_{MD} are presented in turn in Figures 13d, e, f. The terms from turbulent induction (P_{FS} and P_{FA}) contribute to roughly half of the total balance, with the remainder carried by ohmic diffusion of the mean fields (P_{MD}). In the core of the wreathes, removal of mean toroidal field is largely accomplished by fluctuating advection P_{FA} (Fig. 13e) and mean ohmic diffusion P_{MD} (Fig. 13f), with the latter also important near the upper boundary. Turbulent shear becomes strongest near the bottom of the convection zone and in the regions near the high-latitude side of each wreath. Thus P_{FS} (Fig. 13d) becomes the dominant member of the triad of terms seeking to diminish the mean toroidal field there. We find that the mean poloidal field is regenerated in roughly the same region.

In the analysis presented in Figure 13 we have neglected the advection of $\langle B_\phi \rangle$ by the meridional circulations (shown in the Appendix as P_{MA}), which we find plays a very small role in the overall balance. We have also neglected the amplification of $\langle B_\phi \rangle$ by compressibility effects (the Appendix, P_{MC} and P_{FC}), though it does contribute slightly to reinforcing the underlying mean fields within the wreathes.

To summarize, the mean toroidal fields are built through an Ω -effect, where production by the mean shearing flow of differential rotation (P_{MS}) builds the underlying $\langle B_\phi \rangle$. In the

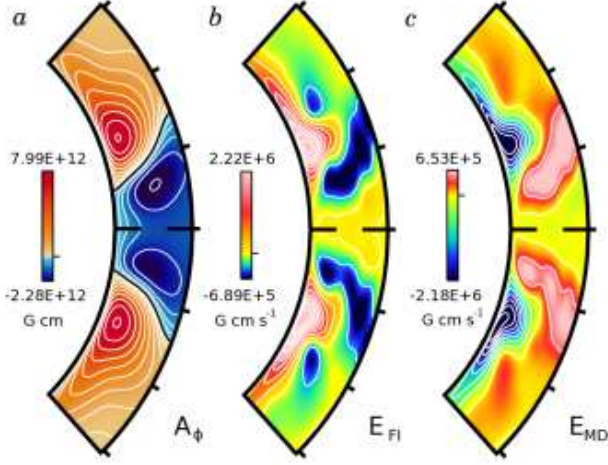


FIG. 14.— Production of mean poloidal vector potential $\langle A_\phi \rangle$ in case D3, with view restricted to $\pm 45^\circ$ latitude. (a) Mean poloidal vector potential $\langle A_\phi \rangle$, with sense denoted by color (red, clockwise; blue, counter-clockwise). (b) The fluctuating (turbulent) emf E_{FI} acts to build the vector potential. This term is strongest near the bottom of the convection zone and the poleward side of the wreathes. (c) Mean ohmic diffusion E_{MD} acts everywhere in opposition to E_{FI} . The cores of the wreathes are positioned at roughly $\pm 15^\circ$ latitude (Fig. 13a).

statistically steady state achieved, this production is balanced by a combination of turbulent induction ($P_{FS} + P_{FA}$) and ohmic diffusion of the mean fields (P_{MD}).

7.2. Maintaining the Poloidal Field

The production of mean poloidal field is achieved through a slightly different balance, with turbulent induction producing poloidal field and ohmic diffusion acting to dissipate it. The mean flows play little role in the overall balance. This balance is clarified if we represent the mean poloidal field by its vector potential $\langle A_\phi \rangle$, where

$$\langle B_{\text{pol}} \rangle = \langle B_r \rangle \hat{r} + \langle B_\theta \rangle \hat{\theta} = \nabla \times \langle A_\phi \hat{\phi} \rangle, \quad (27)$$

as discussed in the Appendix. We recast the induction equation (4) in terms of the poloidal vector potential by uncurling the equation once, obtaining

$$\frac{\partial \langle A_\phi \rangle}{\partial t} = \langle v \times B \rangle|_\phi - \eta \nabla \times \langle B \rangle|_\phi, \quad (28)$$

which is also equation (A29) in the Appendix. The first term is the electromotive force (emf) arising from the coupling of flows and magnetic fields, and the second term is the ohmic diffusion. These can be decomposed into contributions from mean and fluctuating components, as shown symbolically in equation (A30).

In case D3 we find that the mean poloidal vector potential $\langle A_\phi \rangle$ is produced by the fluctuating (turbulent) emf and is dissipated by ohmic diffusion

$$\frac{\partial \langle A_\phi \rangle}{\partial t} \approx E_{FI} + E_{MD} \approx 0. \quad (29)$$

with E_{FI} the emf arising from fluctuating flows and fluctuating fields, and contributing to the mean induction. The E_{MD} is the emf arising from mean ohmic diffusion. These terms are

$$E_{FI} = \langle v' \times B' \rangle|_\phi = \langle v'_r B'_\theta \rangle - \langle v'_\theta B'_r \rangle, \quad (30)$$

$$E_{MD} = -\eta \nabla \times \langle B \rangle|_\phi. \quad (31)$$

The contribution arising from the omitted term E_{MI} (see eq. A31), related to the emf of mean flows and mean fields, is smaller than these first two by more than an order of magnitude. Additionally, E_{MI} has a complicated spatial structure which does not appear to act in a coherent fashion within the wreathes to either build or destroy mean poloidal field.

The mean vector potential $\langle A_\phi \rangle$ is shown in Figure 14a, with poloidal field lines represented by the overlying contours. The mean radial magnetic field $\langle B_r \rangle$ is about ± 1 kG in the cores of the wreathes, whereas the mean colatitudinal field $\langle B_\theta \rangle$ has an amplitude of roughly -2 kG (thus directed northward in both hemispheres), concentrated near the bottom of the convection zone.

The production of $\langle A_\phi \rangle$ by the fluctuating (turbulent) emf E_{FI} is shown in Figure 14b. Here too we average over the same 450 day interval. This term generally acts to reinforce the existing poloidal field, having the same sense as the underlying vector potential in most regions. It is strongest near the bottom of the convection zone and is concentrated at the poleward side of each wreath. This is similar, though not identical, to the structure of destruction of mean toroidal field by fluctuating shear P_{FS} (Fig. 13d). It suggests that mean toroidal field is here being converted into mean poloidal field by the fluctuating flows.

There are two terms that contribute to E_{FI} , as shown in equation (30). Much of that fluctuating emf arises from correlations between fluctuating latitudinal flows and radial fields $\langle -v'_\theta B'_r \rangle$, which follows the structure of E_{FI} (Fig. 14b) closely. The contribution from fluctuating radial flows and colatitudinal fields $\langle v'_r B'_\theta \rangle$ is more complex in structure. Near $\pm 20^\circ$ latitude, this term reinforces $\langle -v'_\theta B'_r \rangle$, but acts against it at higher latitudes and thus diminishes the overall amplitude of E_{FI} . The mean ohmic diffusion E_{MD} (Fig. 14c), almost entirely balances the production of $\langle A_\phi \rangle$ by E_{FI} .

This shows that our mean poloidal magnetic field is maintained by the fluctuating (turbulent) emf and is destroyed by ohmic diffusion. In mean-field dynamo theory, this is often parametrized by an “ α -effect.” Now we turn to interpretations within that framework.

7.3. Exploring Mean-Field Interpretations

Many mean-field theories assert that the production of mean poloidal field is likely to arise from the fluctuating emf. This process is often approximated with an α -effect, where it is proposed that the sense and amplitude of the emf scales with the mean toroidal field

$$\langle v' \times B' \rangle = \alpha \langle B \rangle, \quad (32)$$

where α can be either a simple scalar or may be related to the kinetic and magnetic (current) helicities. In isotropic (but not reflectionally symmetric), homogeneous, incompressible MHD turbulence

$$\alpha = \frac{\tau}{3} (\alpha_k + \alpha_m), \quad (33)$$

$$\alpha_k = -v' \cdot (\nabla \times v'), \quad (34)$$

$$\alpha_m = \frac{1}{4\pi\rho} B' \cdot (\nabla \times B'), \quad (35)$$

as discussed in Pouquet et al. (1976) and Brandenburg & Subramanian (2005). Here τ is the lifetime or correlation time of a typical turbulent eddy. In mean-field theory, these fluctuating helicities are typically not solved directly and are instead solved through auxiliary

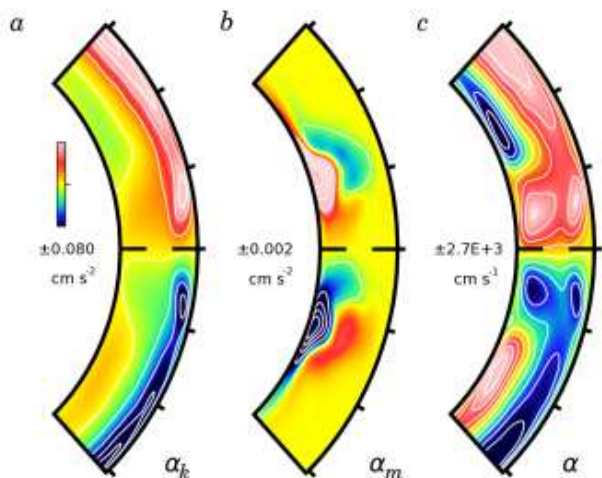


FIG. 15.— Estimating the mean-field α -effect from case D3. (a) Fluctuating kinetic helicity α_k . (b) Fluctuating magnetic (current) helicity α_m . (c) Mean-field α , constructed by combining α_k and α_m with a turbulent correlation time τ .

equations for the total magnetic helicity or are prescribed. Here we can directly measure our fluctuating helicities and examine whether they approximate our fluctuating emf.

To assess the possible role of an α -effect in our simulation, we show in Figures 15a,b the fluctuating kinetic and current helicities α_k and α_m realized in our case D3, averaged over the same 450 day analysis interval. To make an estimate of the α -effect, we approximate the correlation time τ by defining

$$\tau = \frac{H_P}{v'} \quad (36)$$

where H_P is the local pressure scale height and v' is the local fluctuating rms velocity, which are functions of radius only. Estimated by this method, the turnover time τ has a smooth radial profile and is roughly 10 days near the bottom of the convection zone, 3 days at mid-convection zone, and slightly less near the upper boundary. If we use the fast peak upflow or downflow velocities instead of the rms velocities, our estimate of τ is about a factor of 4 smaller. Our mean-field α (eq. 33) is shown in Figure 15c. In the upper convection zone, this is dominated by the fluctuating kinetic helicity while the fluctuating magnetic (current) helicity becomes important at depth.

We form a mean-field emf (right-hand side of eq. 32) by multiplying our derived α (Fig. 15c) with our $\langle B_\phi \rangle$ (Fig. 13a), and show this in Figure 16a. The turbulent emf E_{FI} , which is the left-hand side of equation (32), can be measured in our simulations and is shown again in Figure 16b. Although there is some correspondence in the two patterns, there are significant differences. In particular, the mean-field emf has peak amplitudes in the cores of the wreathes (at $\pm 15^\circ$ latitude) and is negative there. In contrast, the actual fluctuating emf given by E_{FI} is positive and has its highest amplitude at the poleward side of the wreathes. Thus the mean-field emf predicts an incorrect balance in the generation terms and would yield a distinctly different mean poloidal magnetic field. To assess whether better agreement may be achieved with a latitude-averaged emf, we average the mean-field emf and E_{FI} separately over the northern and southern hemispheres and plot these quantities in Figure 16c. Though both have a similar positive sense near the base of the convection zone, the hemisphere-averaged E_{FI} becomes small above

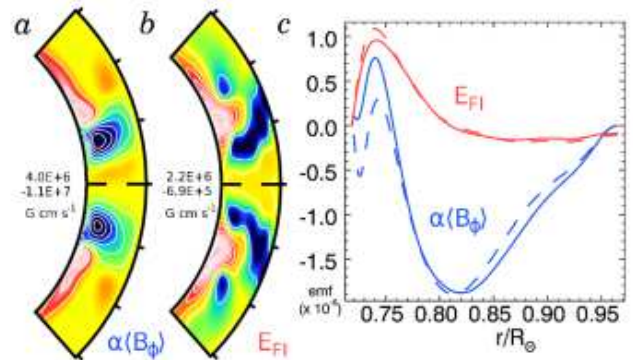


FIG. 16.— Comparison of emfs in case D3. (a) Profile of proposed mean-field emf given by $\alpha\langle B_\phi \rangle$. (b) Actual turbulent emf E_{FI} measured in the dynamo. (c) Variation of hemisphere-averaged emfs with fractional radius. The mean-field approximated emf is shown in blue, and E_{FI} in red. The average over the northern hemisphere is shown solid, the southern is dashed.

$0.8R_\odot$ whereas the averaged mean-field emf $\alpha\langle B_\phi \rangle$ is large and negative there. Thus even the averaged emfs are not in accord.

In summary, it is evident that a simple scalar α -effect will predict the wrong sign for the fluctuating emf in the two hemispheres, as $\langle B_\phi \rangle$ is anti-symmetric across the equator while $\langle A_\phi \rangle$ is symmetric. An α -effect based on the kinetic helicity and magnetic helicity may capture some sense of the fluctuating emf, as those quantities are themselves anti-symmetric across the equator. Yet Figure 16 suggests that there are significant discrepancies between this particular approximation and our turbulent emf. In particular, this mean-field α -effect misses the offset between the generation regions for mean toroidal and mean poloidal field. This offset in latitude of the generation regions may be important for avoiding the α -quenching problems encountered in many mean-field theories. A more complex mean-field model, which takes spatial gradients of $\langle B_\phi \rangle$ into account, may do better. In particular, the $\Omega \times J$ -effect (e.g., Moffatt & Proctor 1982; Rogachevskii & Kleeorin 2003) may be at work in these systems, and preliminary explorations indicate that this term matches the spatial structure of our E_{FI} better than the above α -effect. A tensor representation of the α -effect may do much better, and test-field techniques could be employed to measure this quantity (e.g., Schinnerer et al. 2005, and recently reviewed in Brandenburg 2009).

8. CONCLUSIONS

The ability for a dynamo to build wreathes of strong magnetic fields in the bulk of the convection zone has largely been a surprise, for it had generally been supposed that turbulent convection would disrupt such magnetic structures. To avoid these difficulties, many solar and stellar dynamo theories shift the burden of magnetic storage, amplification and organization to a tachocline of shear and penetration at the base of the convection zone where motions are more quiescent. In contrast, our simulations of rapidly rotating stars are able to achieve sustained global-scale dynamo action within the convection zone itself, with the magnetic structures both being built and able to survive while embedded deep within the turbulence. These dynamos are able to circumvent the Parker instability by means of turbulent Reynolds and Maxwell stresses that contribute to the mechanical force balance and prevent the wreathes from buoyantly escaping the convection zone. This striking behavior may be enabled by the stars rotating three to five times faster than the current Sun,

which yields a strong differential rotation that is a key element in the dynamo behavior. It is quite interesting that in our dynamo cases the angular velocity contrast in latitude and radius is almost constant at differing rotation rates, whereas our hydrodynamic cases tend to have increasing $\Delta\Omega$ with more rapid rotation Ω_0 .

We have achieved some dynamo states that are persistent and others that flip the sense of their magnetic fields. In our case D3 the global-scale fields have small vacillations in their amplitudes, but the magnetic wreathes retain their identities for many thousands of days. This represents hundreds of rotation periods and several magnetic diffusion times, indicating that the dynamo has achieved a persistent equilibrium. Increasing the rotation rate yields more complex time dependence. In our case D5 the oscillations can become large, and may result in the global-scale fields repeatedly flipping their polarity. At times this dynamo appears to be cyclic but in other intervals it behaves more chaotically.

In our persistent case D3 we are able to analyze the generation and transport of mean magnetic field. We find that our dynamo action is of an $\alpha - \Omega$ nature, with the mean toroidal fields being generated by an Ω -effect from the mean shearing flow of differential rotation. This generation is balanced by a combination of turbulent induction and ohmic diffusion. The mean poloidal fields are generated by an α -effect arising from couplings between the fluctuating flows and fluctuating fields, with this production largely balanced by the ohmic diffusion. This is unlike the toroidal balance, for here the mean flows play almost no role and the turbulent correlations are constructive rather than destructive. In assessing what a mean-field model might predict for the magnetic structures realized in case D3, we find that the isotropic, homogeneous α -effect based on kinetic and magnetic (current) helicities fails to capture the sense of our turbulent emf. In general, our E_{FI} is poorly represented by an $\alpha\langle B_\phi \rangle$ that is so determined.

The transition to richer time dependence with increasing rotation rate in case D5 appears to arise from subtle changes and phasing relationships between the toroidal and poloidal magnetic production terms. These are difficult to assess, since the production terms themselves are complex in space and now vary in time as well. It is evident that the mean poloidal fields lag the changes in the mean toroidal fields, and there is clear migration of magnetic field to the higher latitudes during a reversal. This latitudinal migration may result from a polarward-slip instability, triggered by the stronger magnetic fields that are generated by this dynamo, and this migration may lead to the oscillations in field strength and polarity. The analysis of magnetic field production that we have carried out for case D3 required significant averaging of the turbulent correlations, accomplished here by time averages, to obtain a coherent picture of the balances achieved. This has not yet been tractable for the oscillating solutions, as the generation terms change on shorter time scales than needed to obtain stable averages of the turbulent processes. It appears that the imbalances in the production and destruction of mean magnetic fields during cyclic behavior are modest, and currently we cannot pinpoint just which terms out of the large medley serve to drive the oscillations.

These dynamo oscillations are not special to case D5. Indeed, we have explored a broader class of oscillating dynamo solutions, which will be reported in a subsequent paper. Some of these solutions are realized by taking our more slowly rotating case D3 to higher levels of turbulence by reducing the

eddy diffusivities, while others are achieved at even higher rotation rates. We find such global-scale oscillations and polarity reversals fascinating, since these appear to be the first self-consistent 3-D stellar dynamo simulations which achieve such temporally organized behavior in the bulk of the convection zone.

Accompanying the oscillations in global-scale magnetic field are changes in the differential rotation, and these signatures are the most likely to be found through stellar observations. The angular velocity contrast $\Delta\Omega_{\text{lat}}$ between the equator and high latitudes can vary by 20% over periods of hundreds or thousands of days. The patterns of speedup which we find propagating toward the polar regions of these dynamos may have correspondence with the polar branch of the torsional oscillations which are observed in the Sun. The speedup features may arise from conservation of angular momentum in fluid which is partially trapped within the wreathes as they slip toward the poles. The leaky nature of our wreathes will modify this somewhat and that may explain why the wreathes are not stabilized by rotation (e.g., Moreno-Insertis et al. 1992).

The realization of global-scale magnetic structures in our simulations, and their great strength relative to the fluctuating fields, may in part be a consequence of the relatively modest degree of turbulence attained here. Whether such structures can be generated and sustained amidst the far more complex flows in actual stellar interiors is not yet clear. If such structures are indeed realized in stars, they may or may not survive to print through the highly turbulent convection occurring just below the stellar photosphere. If they do appear at the surface, some global-scale magnetic features may propagate toward the poles along with the bands of angular velocity speedup. There are some indications in stellar observations that global-scale toroidal magnetic fields may indeed become strong in rapidly rotating stars (Donati et al. 2006; Petit et al. 2008), though small-scale fields may still account for much of the magnetic energy near the surface (Reiners & Basri 2009). The global-scale poloidal fields may be more successful in surviving the passage through the turbulent surface convection. If they do, the stellar magnetic field will likely have significant non-dipole components. Thus the mean poloidal fields observed at the surface may give clues to the presence of large wreathes of magnetism that occupy the bulk of the convection zone.

We thank Axel Brandenburg, Geoffrey Vasil and Steve Saar for helpful conversations and advice about stellar magnetism and dynamo action. This research is supported by NASA through Heliophysics Theory Program grants NNG05G124G and NNX08AI57G, with additional support for Brown through the NASA GSRP program by award number NNG05GN08H. Browning was supported by a NSF Astronomy and Astrophysics postdoctoral fellowship AST 05-02413, and now by research support at CITA. Brun was partly supported by the Programme National Soleil-Terre of CNRS/INSU (France), and by the STARS2 grant from the European Research Council. The simulations were carried out with NSF PACI support of PSC, SDSC, TACC and NCSA, and by NASA HEC support at Project Columbia. Volume renderings used in the analysis and the field line tracings shown were produced using VAPOR (Clyne et al. 2007).

APPENDIX

PRODUCTION, DESTRUCTION AND TRANSPORT OF MAGNETIC FIELD

We derive diagnostic tools to evaluate the generation and transport of magnetic field in a magnetized and rotating turbulent convection zone. This derivation is in spherical coordinates, and is under the anelastic approximation.

Induction Equation

In the induction equation (4), the first term on the right hand side represents production of magnetic field while the second term represents its diffusion. We first rewrite the production term to make the contributions of shear, advection and compressible effects more explicit as

$$\nabla \times (v \times B) = (B \cdot \nabla)v - (v \cdot \nabla)B - B(\nabla \cdot v). \quad (\text{A1})$$

Under the anelastic approximation the divergence of v can be expressed in terms of the logarithmic derivative of the mean density because

$$\nabla \cdot (\bar{\rho}v) = 0 = \bar{\rho}(\nabla \cdot v) + (v \cdot \nabla)\bar{\rho},$$

and therefore

$$\nabla \cdot v = -v_r \frac{\partial}{\partial r} \ln \bar{\rho}. \quad (\text{A2})$$

The induction equation thus becomes

$$\frac{\partial B}{\partial t} = \underbrace{(B \cdot \nabla)v}_{\text{shearing}} - \underbrace{(v \cdot \nabla)B}_{\text{advection}} + \underbrace{v_r B \frac{\partial}{\partial r} \ln \bar{\rho}}_{\text{compression}} - \underbrace{\nabla \times (\eta \nabla \times B)}_{\text{diffusion}} \quad (\text{A3})$$

As labeled, the first term represents shearing of B , the second term advection of B , the third one compressible amplification of B , and the last term ohmic diffusion.

Production of Axisymmetric Magnetic Field

To identify the processes contributing to the production of mean (axisymmetric) field, we separate our velocities and magnetic fields into mean and fluctuating components $v = \langle v \rangle + v'$ and $B = \langle B \rangle + B'$ where angle brackets denote an average in longitude. Thus $\langle v' \rangle = \langle B' \rangle = 0$ by definition. Expanding the production term of equation (A3) we obtain the mean shearing term

$$\langle (B \cdot \nabla)v \rangle = (\langle B \rangle \cdot \nabla) \langle v \rangle + \langle (B' \cdot \nabla)v' \rangle, \quad (\text{A4})$$

the mean advection term

$$-\langle (v \cdot \nabla)B \rangle = -(\langle v \rangle \cdot \nabla) \langle B \rangle - \langle (v' \cdot \nabla)B' \rangle, \quad (\text{A5})$$

and the mean compressibility term

$$\langle v_r B \frac{\partial}{\partial r} \ln \bar{\rho} \rangle = (\langle v_r \rangle \langle B \rangle + \langle v'_r B' \rangle) \frac{\partial}{\partial r} \ln \bar{\rho}. \quad (\text{A6})$$

In a similar fashion, the mean diffusion term becomes

$$-\langle \nabla \times (\eta \nabla \times B) \rangle = -\nabla \times (\eta \nabla \times \langle B \rangle). \quad (\text{A7})$$

The axisymmetric component of the induction equation is written symbolically as:

$$\frac{\partial \langle B \rangle}{\partial t} = P_{\text{MS}} + P_{\text{FS}} + P_{\text{MA}} + P_{\text{FA}} + P_{\text{MC}} + P_{\text{FC}} + P_{\text{MD}} \quad (\text{A8})$$

With P_{MS} representing production of field by mean shear, P_{FS} production by fluctuating shear, P_{MA} advection by mean flows, P_{FA} advection by fluctuating flows, P_{MC} amplification arising from the compressibility of mean flows, P_{FC} amplification arising from fluctuating compressible motions, and P_{MD} ohmic diffusion of the mean fields. In turn, these terms are

$$\begin{aligned} P_{\text{MS}} &= (\langle B \rangle \cdot \nabla) \langle v \rangle, & P_{\text{FS}} &= \langle (B' \cdot \nabla)v' \rangle, & P_{\text{MA}} &= -(\langle v \rangle \cdot \nabla) \langle B \rangle, & P_{\text{FA}} &= -\langle (v' \cdot \nabla)B' \rangle, \\ P_{\text{MC}} &= (\langle v_r \rangle \langle B \rangle) \frac{\partial}{\partial r} \ln \bar{\rho}, & P_{\text{FC}} &= \langle (v'_r B') \rangle \frac{\partial}{\partial r} \ln \bar{\rho}, \text{ and} & P_{\text{MD}} &= -\nabla \times (\eta \nabla \times \langle B \rangle). \end{aligned} \quad (\text{A9})$$

We now expand each of these terms into their full representation in spherical coordinates.

Production of Mean Longitudinal Field

$$\frac{\partial \langle B_\phi \rangle}{\partial t} = P_{MS} + P_{FS} + P_{MA} + P_{FA} + P_{MC} + P_{FC} + P_{MD}$$

$$P_{MS} = \left[\langle B_r \rangle \frac{\partial}{\partial r} + \frac{\langle B_\theta \rangle}{r} \frac{\partial}{\partial \theta} \right] \langle v_\phi \rangle + \frac{\langle B_\phi \rangle \langle v_r \rangle + \cot \theta \langle B_\phi \rangle \langle v_\theta \rangle}{r} \quad (A10)$$

$$P_{FS} = \left\langle \left[B'_r \frac{\partial}{\partial r} + \frac{B'_\theta}{r} \frac{\partial}{\partial \theta} + \frac{B'_\phi}{r \sin \theta} \frac{\partial}{\partial \phi} \right] v'_\phi \right\rangle + \frac{\langle B'_\phi v'_r \rangle + \cot \theta \langle B'_\phi v'_\theta \rangle}{r} \quad (A11)$$

$$P_{MA} = - \left[\langle v_r \rangle \frac{\partial}{\partial r} + \frac{\langle v_\theta \rangle}{r} \frac{\partial}{\partial \theta} \right] \langle B_\phi \rangle - \frac{\langle v_\phi \rangle \langle B_r \rangle + \cot \theta \langle v_\phi \rangle \langle B_\theta \rangle}{r} \quad (A12)$$

$$P_{FA} = - \left\langle \left[v'_r \frac{\partial}{\partial r} + \frac{v'_\theta}{r} \frac{\partial}{\partial \theta} + \frac{v'_\phi}{r \sin \theta} \frac{\partial}{\partial \phi} \right] B'_\phi \right\rangle - \frac{\langle v'_\phi B'_r \rangle + \cot \theta \langle v'_\phi B'_\theta \rangle}{r} \quad (A13)$$

$$P_{MC} = (\langle v_r \rangle \langle B_\phi \rangle) \frac{\partial}{\partial r} \ln \bar{\rho} \quad P_{FC} = (\langle v'_r B'_\phi \rangle) \frac{\partial}{\partial r} \ln \bar{\rho} \quad (A14)$$

$$P_{MD} = \eta \nabla^2 \langle B_\phi \rangle - \frac{\eta \langle B_\phi \rangle}{r^2 \sin^2 \theta} + \frac{d\eta}{dr} \left(\frac{1}{r} \frac{\partial (r \langle B_\phi \rangle)}{\partial r} \right) \quad (A15)$$

Production of Mean Latitudinal Field

$$\frac{\partial \langle B_\theta \rangle}{\partial t} = P_{MS} + P_{FS} + P_{MA} + P_{FA} + P_{MC} + P_{FC} + P_{MD}$$

$$P_{MS} = \left[\langle B_r \rangle \frac{\partial}{\partial r} + \frac{\langle B_\theta \rangle}{r} \frac{\partial}{\partial \theta} \right] \langle v_\theta \rangle + \frac{\langle B_\theta \rangle \langle v_r \rangle - \cot \theta \langle B_\phi \rangle \langle v_\phi \rangle}{r} \quad (A16)$$

$$P_{FS} = \left\langle \left[B'_r \frac{\partial}{\partial r} + \frac{B'_\theta}{r} \frac{\partial}{\partial \theta} + \frac{B'_\phi}{r \sin \theta} \frac{\partial}{\partial \phi} \right] v'_\theta \right\rangle + \frac{\langle B'_\theta v'_r \rangle - \cot \theta \langle B'_\phi v'_\phi \rangle}{r} \quad (A17)$$

$$P_{MA} = - \left[\langle v_r \rangle \frac{\partial}{\partial r} + \frac{\langle v_\theta \rangle}{r} \frac{\partial}{\partial \theta} \right] \langle B_\theta \rangle - \frac{\langle v_\theta \rangle \langle B_r \rangle - \cot \theta \langle v_\phi \rangle \langle B_\phi \rangle}{r} \quad (A18)$$

$$P_{FA} = - \left\langle \left[v'_r \frac{\partial}{\partial r} + \frac{v'_\theta}{r} \frac{\partial}{\partial \theta} + \frac{v'_\phi}{r \sin \theta} \frac{\partial}{\partial \phi} \right] B'_\theta \right\rangle - \frac{\langle v'_\theta B'_r \rangle - \cot \theta \langle v'_\phi B'_\phi \rangle}{r} \quad (A19)$$

$$P_{MC} = (\langle v_r \rangle \langle B_\theta \rangle) \frac{\partial}{\partial r} \ln \bar{\rho} \quad P_{FC} = (\langle v'_r B'_\theta \rangle) \frac{\partial}{\partial r} \ln \bar{\rho} \quad (A20)$$

$$P_{MD} = \eta \nabla^2 \langle B_\theta \rangle + \frac{2\eta}{r^2} \frac{\partial \langle B_r \rangle}{\partial \theta} - \frac{\eta \langle B_\theta \rangle}{r^2 \sin^2 \theta} + \frac{d\eta}{dr} \left(\frac{1}{r} \frac{\partial (r \langle B_\theta \rangle)}{\partial r} - \frac{1}{r} \frac{\partial \langle B_r \rangle}{\partial \theta} \right) \quad (A21)$$

Production of Mean Radial Field

$$\frac{\partial \langle B_r \rangle}{\partial t} = P_{MS} + P_{FS} + P_{MA} + P_{FA} + P_{MC} + P_{FC} + P_{MD}$$

$$P_{MS} = \left[\langle B_r \rangle \frac{\partial}{\partial r} + \frac{\langle B_\theta \rangle}{r} \frac{\partial}{\partial \theta} \right] \langle v_r \rangle - \frac{\langle B_\theta \rangle \langle v_\theta \rangle + \langle B_\phi \rangle \langle v_\phi \rangle}{r} \quad (A22)$$

$$P_{FS} = \left\langle \left[B'_r \frac{\partial}{\partial r} + \frac{B'_\theta}{r} \frac{\partial}{\partial \theta} + \frac{B'_\phi}{r \sin \theta} \frac{\partial}{\partial \phi} \right] v'_r \right\rangle - \frac{\langle B'_\theta v'_\theta \rangle + \langle B'_\phi v'_\phi \rangle}{r} \quad (A23)$$

$$P_{MA} = - \left[\langle v_r \rangle \frac{\partial}{\partial r} + \frac{\langle v_\theta \rangle}{r} \frac{\partial}{\partial \theta} \right] \langle B_r \rangle + \frac{\langle v_\theta \rangle \langle B_\theta \rangle + \langle v_\phi \rangle \langle B_\phi \rangle}{r} \quad (A24)$$

$$P_{FA} = - \left\langle \left[v'_r \frac{\partial}{\partial r} + \frac{v'_\theta}{r} \frac{\partial}{\partial \theta} + \frac{v'_\phi}{r \sin \theta} \frac{\partial}{\partial \phi} \right] B'_r \right\rangle + \frac{\langle v'_\theta B'_\theta \rangle + \langle v'_\phi B'_\phi \rangle}{r} \quad (A25)$$

$$P_{MC} = (\langle v_r \rangle \langle B_r \rangle) \frac{\partial}{\partial r} \ln \bar{\rho} \quad P_{FC} = (\langle v'_r B'_r \rangle) \frac{\partial}{\partial r} \ln \bar{\rho} \quad (A26)$$

$$P_{MD} = \eta \nabla^2 \langle B_r \rangle - 2\eta \frac{\langle B_r \rangle}{r^2} - \frac{2\eta}{r^2} \frac{\partial \langle B_\theta \rangle}{\partial \theta} - \frac{2\eta \cot \theta \langle B_\theta \rangle}{r^2} \quad (A27)$$

Maintaining the Poloidal Vector Potential

The balances achieved in maintaining the mean poloidal magnetic field are somewhat clearer if we consider its vector potential rather than the fields themselves. The mean poloidal field $\langle B_{\text{pol}} \rangle$ has a corresponding vector potential $\langle A_{\phi} \rangle$, where

$$\begin{aligned} \langle B_{\text{pol}} \rangle &= \langle B_r \rangle \hat{r} + \langle B_{\theta} \rangle \hat{\theta} = \nabla \times \langle A_{\phi} \rangle \\ &= \frac{1}{r \sin \theta} \frac{\partial}{\partial \theta} \langle A_{\phi} \sin \theta \rangle \hat{r} - \frac{1}{r} \frac{\partial}{\partial r} \langle r A_{\phi} \rangle \hat{\theta} \\ &= \nabla \times \langle A_{\phi} \hat{\phi} \rangle. \end{aligned} \quad (\text{A28})$$

The other components of the poloidal vector potential disappear, as terms involving $\partial/\partial\phi$ vanish in the azimuthally-averaged equations. Likewise, the ϕ -component of the possible gauge term $\nabla\lambda$ is zero by virtue of axisymmetry. We recast the induction equation (eq. 4) in terms of the poloidal vector potential by uncurling the equation once and obtain

$$\frac{\partial \langle A_{\phi} \rangle}{\partial t} = v \times B|_{\phi} - \eta \nabla \times B|_{\phi}. \quad (\text{A29})$$

This can then be decomposed into mean and fluctuating contributions, and represented symbolically as

$$\frac{\partial \langle A_{\phi} \rangle}{\partial t} = E_{\text{MI}} + E_{\text{FI}} + E_{\text{MD}}, \quad (\text{A30})$$

with E_{MI} representing the electromotive forces (emf) arising from mean flows and mean fields, and related to their mean induction. Likewise, E_{FI} is the emf from fluctuating flows and fields and E_{MD} is the emf arising from mean diffusion. These are in turn

$$E_{\text{MI}} = \langle v \rangle \times \langle B \rangle|_{\phi} = \langle v_r \rangle \langle B_{\theta} \rangle - \langle v_{\theta} \rangle \langle B_r \rangle, \quad (\text{A31})$$

$$E_{\text{FI}} = \langle v' \times B' \rangle|_{\phi} = \langle v'_r B'_{\theta} \rangle - \langle v'_{\theta} B'_r \rangle, \quad (\text{A32})$$

$$E_{\text{MD}} = -\eta \nabla \times \langle B \rangle|_{\phi} = -\eta \frac{1}{r} \left(\frac{\partial}{\partial r} (r \langle B_{\theta} \rangle) - \frac{\partial \langle B_r \rangle}{\partial \theta} \right) \quad (\text{A33})$$

Fluctuating (Non-Axisymmetric) Component of the Induction Equation

Left out of this analysis is the fluctuating component of the induction equation. This can be derived by subtracting the mean induction equation (A8) from the full induction equation, yielding the following equation for the fluctuating fields

$$\begin{aligned} \frac{\partial B'}{\partial t} &= (\langle B \rangle \cdot \nabla) v' + (B' \cdot \nabla) \langle v \rangle + \mathcal{E} \\ &\quad - (\langle v \rangle \cdot \nabla) B' - (v' \cdot \nabla) \langle B \rangle - \mathcal{F} \\ &\quad + (\langle v_r \rangle B' + v'_r \langle B \rangle) \frac{\partial}{\partial r} \ln \bar{\rho} + \mathcal{G} \\ &\quad - \nabla \times (\eta \nabla \times \langle B' \rangle) \end{aligned} \quad (\text{A34})$$

where the quantities $\mathcal{E} = (B' \cdot \nabla) v' - (\langle B' \cdot \nabla \rangle v')$, $\mathcal{F} = (v' \cdot \nabla) B' - \langle (v' \cdot \nabla) B' \rangle$, and $\mathcal{G} = (v'_r B' - \langle v'_r B' \rangle) \frac{\partial}{\partial r} \ln \bar{\rho}$, represent the difference between mixed stresses from which we subtract their axisymmetric mean. In the standard mean-field derivation, these quantities are siblings of the G-current involving the mean electromotive force $\langle v \times B \rangle$ and its 3-D equivalent $v \times B$ (i.e., the so called ‘‘pain in the neck’’ term, Moffatt 1978).

REFERENCES

- Baliunas, S., Sokoloff, D., & Soon, W. 1996, *ApJ*, 457, L99
 Barnes, S. A. 2003, *ApJ*, 586, 464
 Bouvier, J., Forestini, M., & Allain, S. 1997, *A&A*, 326, 1023
 Brandenburg, A. 2009, *Space Science Reviews*, 144, 87
 Brandenburg, A. & Subramanian, K. 2005, *Phys. Rep.*, 417, 1
 Brown, B. P., Browning, M. K., Brun, A. S., Miesch, M. S., & Toomre, J. 2008, *ApJ*, 689, 1354
 Browning, M. K. 2008, *ApJ*, 676, 1262
 Browning, M. K., Miesch, M. S., Brun, A. S., & Toomre, J. 2006, *ApJ*, 648, L157
 Brun, A. S., Antia, H. M., Chitre, S. M., & Zahn, J.-P. 2002, *A&A*, 391, 725
 Brun, A. S., Browning, M. K., & Toomre, J. 2005, *ApJ*, 629, 461
 Brun, A. S., Miesch, M. S., & Toomre, J. 2004, *ApJ*, 614, 1073
 Busse, F. H. 1970, *Journal of Fluid Mechanics*, 44, 441
 Charbonneau, P. & MacGregor, K. B. 1997, *ApJ*, 486, 502
 Cline, K. S., Brummell, N. H., & Cattaneo, F. 2003, *ApJ*, 588, 630
 Clune, T. L., Elliott, J. R., Glatzmaier, G. A., Miesch, M. S., & Toomre, J. 1999, *Parallel Computing*, 25, 361
 Clyne, J., Mininni, P., Norton, A., & Rast, M. 2007, *New Journal of Physics*, 9, 301
 Delfosse, X., Forveille, T., Perrier, C., & Mayor, M. 1998, *A&A*, 331, 581
 Donati, J.-F., Forveille, T., Cameron, A. C., Barnes, J. R., Delfosse, X., Jardine, M. M., & Valenti, J. A. 2006, *Science*, 311, 633
 James, D. J., Jardine, M. M., Jeffries, R. D., Randich, S., Collier Cameron, A., & Ferreira, M. 2000, *MNRAS*, 318, 1217
 Jouve, L. & Brun, A. S. 2009, *ApJ*, submitted
 Käpylä, P. J., Korpi, M. J., & Brandenburg, A. 2009, *ApJ*, 697, 1153
 Knobloch, E., Rosner, R., & Weiss, N. O. 1981, *MNRAS*, 197, 45P
 Leorat, J., Pouquet, A., & Frisch, U. 1981, *Journal of Fluid Mechanics*, 104, 419
 MacGregor, K. B. & Brenner, M. 1991, *ApJ*, 376, 204
 Matt, S. & Pudritz, R. E. 2008, *ApJ*, 678, 1109
 Miesch, M. S., Brun, A. S., & Toomre, J. 2006, *ApJ*, 641, 618
 Moffatt, H. K. 1978, *Magnetic field generation in electrically conducting fluids* (Cambridge, England, Cambridge University Press, 1978. 353 p.)
 Moffatt, H. K. & Proctor, M. R. E. 1982, *Geophysical and Astrophysical Fluid Dynamics*, 21, 265
 Mohanty, S. & Basri, G. 2003, *ApJ*, 583, 451
 Moreno-Insertis, F., Schuessler, M., & Ferriz-Mas, A. 1992, *A&A*, 264, 686

- Noyes, R. W., Hartmann, L. W., Baliunas, S. L., Duncan, D. K., & Vaughan, A. H. 1984, *ApJ*, 279, 763
- Ossendrijver, M. 2003, *A&A Rev.*, 11, 287
- Parker, E. N. 1975, *ApJ*, 198, 205
- . 1993, *ApJ*, 408, 707
- Petit, P., Dintrans, B., Solanki, S. K., Donati, J.-F., Aurière, M., Lignières, F., Morin, J., Paletou, F., Ramirez Velez, J., Catala, C., & Fares, R. 2008, *MNRAS*, 388, 80
- Pizzo, V., Schwenn, R., Marsch, E., Rosenbauer, H., Muehlhaeuser, K.-H., & Neubauer, F. M. 1983, *ApJ*, 271, 335
- Pizzolato, N., Maggio, A., Micela, G., Sciortino, S., & Ventura, P. 2003, *A&A*, 397, 147
- Pouquet, A., Frisch, U., & Leorat, J. 1976, *Journal of Fluid Mechanics*, 77, 321
- Reiners, A. & Basri, G. 2007, *ApJ*, 656, 1121
- . 2009, *A&A*, 496, 787
- Reiners, A., Basri, G., & Browning, M. 2009, *ApJ*, 692, 538
- Rempel, M. 2005, *ApJ*, 622, 1320
- . 2006, *ApJ*, 647, 662
- . 2007, *ApJ*, 655, 651
- Rogachevskii, I. & Kleeorin, N. 2003, *Phys. Rev. E*, 68, 036301
- Saar, S. H. 1996, in *IAU Symposium*, Vol. 176, *Stellar Surface Structure*, ed. K. G. Strassmeier & J. L. Linsky, 237
- Saar, S. H. 2001, in *Astronomical Society of the Pacific Conference Series*, Vol. 223, *11th Cambridge Workshop on Cool Stars, Stellar Systems and the Sun*, ed. R. J. Garcia Lopez, R. Rebolo, & M. R. Zapaterio Osorio, 292
- Schrinner, M., Rädler, K.-H., Schmitt, D., Rheinhardt, M., & Christensen, U. 2005, *Astronomische Nachrichten*, 326, 245
- Skumanich, A. 1972, *ApJ*, 171, 565
- Spruit, H. C. 2003, *Sol. Phys.*, 213, 1
- Spruit, H. C. & van Ballegooijen, A. A. 1982, *A&A*, 106, 58
- Steenbeck, M., Krause, F., & Rädler, K. H. 1966, *Zeitschrift Naturforschung Teil A*, 21, 369
- Thompson, M. J., Christensen-Dalsgaard, J., Miesch, M. S., & Toomre, J. 2003, *ARA&A*, 41, 599
- Vasil, G. M. & Brummell, N. H. 2008, *ApJ*, 686, 709
- . 2009, *ApJ*, 690, 783
- Weber, E. J. & Davis, L. J. 1967, *ApJ*, 148, 217
- West, A. A., Hawley, S. L., Bochanski, J. J., Covey, K. R., Reid, I. N., Dhital, S., Hilton, E. J., & Masuda, M. 2008, *AJ*, 135, 785
- West, A. A., Hawley, S. L., Walkowicz, L. M., Covey, K. R., Silvestri, N. M., Raymond, S. N., Harris, H. C., Munn, J. A., McGehee, P. M., Ivezić, Ž., & Brinkmann, J. 2004, *AJ*, 128, 426